CHARACTERIZATION OF SIGNAL DEGRADATION AND POLARIZATION BACKSCATTER IN LASER-ILLUMINATED SCENES

by

Frances Rosemarie Bodrucki

A dissertation submitted to the faculty of
The University of North Carolina at Charlotte
in partial fulfillment of the requirements
for the degree of Doctor of Philosophy in
Optical Science and Engineering

Charlotte

2019

Approved by:

_____
Dr. Glenn Boreman

_____
Dr. Angela Davies

_____
Dr. Thomas Suleski

_____
Dr. Tino Hofmann

_____
Dr. Menelaos Poutous

_____
Dr. Yvette Huet

ABSTRACT

FRANCES ROSEMARIE BODRUCKI. Characterization of Signal Degradation and Polarization Backscatter in Laser-Illuminated Scenes. (Under the direction of DR. GLENN BOREMAN)

Scenes containing laser illumination are commonly encountered in a variety of remote-sensing applications. One aspect of laser illumination is that it can interfere with electronic image acquisition, especially if it is modulated at temporal frequencies close to the frame rate of the sensing system, or at harmonics or subharmonics of the frame rate. A quantitative measure of this aliasing interference is developed and used to characterize the robustness of the image acquisition and variation of tracker line of sight under various illumination scenarios. A second aspect of laser illumination is that objects present in the scene reflect some flux back to the sensor, often with a change in the polarization characteristics of the radiation. The fact that this change in polarization is a function of the material composition and geometrical configuration of an object can be used to develop discrimination techniques and criteria used to decide the presence or absence of certain classes of objects in the scene, toward the goal of developing an object-classification capability against competing background clutter. From this perspective, polarization characteristics of a number of commonly encountered objects are measured, such as prisms, corner cube reflectors, retroreflective tape, and liquid crystal light modulators that are typically used as laser beam steerers. Laser-based measurements were performed at various angles of incidence, and for the liquid crystals, also as a function of applied voltage. The acquired data sets for these objects are presented in terms of the Mueller matrix. This formalism connects the input and output Stokes

vectors, thus providing a complete polarization signature of each object at the measurement wavelength. We discuss our measured results in the context of previous literature references, for purposes of comparison and cross-validation. Especially for the case of reflection measurements on the liquid crystal light modulators, we believe that the Mueller matrix data sets presented are new contributions to the literature.

ACKNOWLEDGMENTS

Firstly, I would like to thank my advisor for his guidance, patience and understanding through this journey as it was not the most conventional route, nor the smoothest. I would also like to thank Scott Williams for his assistance with the data collection and troubleshooting, as well as being a supportive and kind friend. Thank you to The Scatterworks, Inc. for their assistance with the CASI machine. Thank you to my committee members: Dr. Angela Davies, Dr. Tino Hoffmann, Dr. Thomas Suleski, Dr. Menelaos Poutous, and Dr. Yvette Huet for their support and patience throughout the pursuit of my degree. I would also like to acknowledge the US Army Research Development and Engineering Command (RDECOM) for funding my research and my supervisors Glenda Mendiola, Michael Cannizzaro, John Suarez, Leslie Litten, Joseph Oagaro, Mark Calafut, Wilbur Chin, and Ralph Troisio for their continuing encouragement, support and guidance. To my fellow graduate students: Charlotte Stahl, Joseph Peller, Zeba Naqvi, Ken Allen, Abby Peltier, Alex Rosenthal, Geoffrey Tuttle, Max Burnett, Chris Wilson, Tim Mode, Scott Raburn, Jason Case, Eric Browry, Nasim Habibi, Michael Uwakwe, Navid Farahi and Madison Young, thank you all for your kindness, help and encouragement along this journey. Finally, I would also like to thank my family for their constant encouragement and support.

TABLE OF CONTENTS

LIST OF FIGURES

LIST OF TABLES

LIST OF ABBREVIATIONS

CASI	Complete Angle Scatter Instrument
CCD	charge coupled- device
CCR	cornercube reflector
COTS	commercial-off-the-shelf
FINC	Flicker, Instantaneous Normalized Contrast
HWP	half-waveplate
IR	infrared
LC	Liquid Crystal
QCL	quantum cascade laser
QWP	quarter-waveplate
SUT	subject under test

CHAPTER 1: INTRODUCTION

Multiple technologies across industry, academia and military sectors rely upon both passive and active detection of signals. The applications of these sensor technologies, in both laboratory and field-testing scenarios, range from temperature sensing to motion/proximity detection, and beyond. With a variety of fields related to sensors and sensor components the environment and technologies are rapidly changing and expanding. For these reasons, adaptability is imperative. This need for adaptability is in part why tunable sources (1), such as quantum cascade lasers (QCLs), are becoming more commonly available and utilized. From these advancements, it would follow as a logical step that if sources are adaptable, sensors should be adaptable as well.

As optical sensing technologies become more integrated in various mechanical and electrical systems, it is also essential that the sensors respond accurately to the appropriate signal inputs. This includes rejection of false triggers, as well as the ability to autonomously adjust for maximum responsivity. Issues arise due to situations such as matching/mismatching signal (phasing), detection rates (aliasing), as well as in-scene clutter which include returns from objects such as: driveway reflectors, auto tail lights, large surface areas, aluminum cans, etc.

To address these specific issues, a twofold approach for optimization of laboratory and field-testing capabilities is presented here. The focus of this dissertation is on the optimization of sensors, including characterization of the polarization properties of reflected and transmitted signals, as well as an adaptable frame rate sensor to mitigate aliasing effects. The goals of this research include the study the polarization effect of

reflected and transmitted signals in polarization susceptible materials, as well as optimization of sensor response for data collection processes both in laboratory testing and field-testing scenarios.

Aliasing is defined as an effect that causes different signals to become indistinguishable when sampled. Real world examples of this are the stroboscopic effect, also known as the Wagon Wheel effect, where temporal aliasing is observed due to the periodic flickering of a light source. Various ways to detect and mitigate effects of aliasing have been pursued in the literature. Most mitigation techniques focus on reduction of aliasing (2) rather than negation or avoidance/correction of it, with examples of mitigation ranging from microscanning (3) to filtering (4). The anti-aliasing approach detailed in this dissertation includes determining the aliasing window of various sensors (for both fixed and adjustable frame rate), their fundamental frequencies, harmonics, as well as the development of a MATLAB-based detection algorithm for sensors with adjustable frame to combat aliasing in situ. The research outlined in this dissertation focuses on the identification and mitigation of aliasing via direct frame-to-frame comparison and a feedback loop to autonomously adjust the frame rate to counteract this aliasing. In laboratory and field-testing scenarios, it becomes apparent that while higher frame rates are ideal for data acquisition in certain situations, they might not be feasible for operation in the case of every data collection. For example, in Handa 2012 (5), the following point is made regarding frame rate: a higher frame rate is not always best when dealing with certain scenes, such as that with low lighting levels because the shorter frame time degrades the image signal-to-noise ratio.

The other aspect of the problem considered here, polarization discrimination via Mueller matrix measurements, is supported extensively in the established literature; precedence is set for the exploration of polarization properties of various materials. The necessity for proper signal identification is emphasized in Sjöqvist 2013 (6) where he discusses the importance of discriminating signals of interest and false targets in autonomous sensors. This is especially true in urban settings, where generally the surfaces generate return signals similar to retroreflective targets of interest. The struggle, he notes, in creating autonomous sensors is the need for low false-alarm rates.

In the late 1960s, investigations began into both the polarization of light reflected from natural surfaces (7) and Mueller matrix characteristics of sea water (8) and man-made cornercube reflectors and cavities (9). Retroreflections differ from standard reflections in the angle of their return. The angle of incidence of the incident light is equal to the angle of reflection of the reflected light in standard reflections, whereas with retroreflections the incident light (7) is reflected directly back toward its source.

In the 1970s this progressed to optical augmentation utilizing short pulse lasers has been explored for detection and discrimination purposes (10)(11). A patent for optical augmentation was first filed by Wilbur Liebson in 1978 (12). Optical augmentation utilizes laser pulses, in a manner similar to radar, to determine information about remote optical surfaces or devices, via principles of retroreflection.

Patents from Miller Jr 1980 (13) and Naiman 1989 (14), show optical augmentation utilized for various sensing and guiding applications. Wilson 1995 (15), Gleason 1997 (16), and most recently Reyes 2011 (17) all focus on improvements to optical augmentation sensing technologies. Each patent addresses a different aspect of

improvement, which include excluding off-axis reflections, uses of polarizers, optical rotators and image-processing techniques, all with the end goal of removing erroneous signals from the detection process.

In the 1980s, Mueller matrix methods became useful in the field of biology for identification applications for microorganisms (20), microbials (21), viruses (22), bacterial suspensions (23), and biological particles (24). Mueller matrix methods were also utilized beginning in the 1980s for a variety of radar applications including target discrimination, classification, imaging and identification (25), validation analysis of polarimetric radar returns (26), and mixed target state discrimination techniques (27).

Mueller matrix identification and/or characterization continued to progress into the 1990s for various objects and scenes including seawater and underwater targets (28), contaminant coatings over rough surfaces (29), classification of radar imagery (30), non-homogeneous spherical particles (31), polarization and depolarization properties of optical targets (32), seawater immersed targets (33), and radar polarization target decomposition (34). Up to present day, Mueller matrix spectroscopy is utilized for chemical and biological detection, identification and characterization applications such as for crystalline organics, particularly in the infrared range (35). This includes diagnosing oral precancer (36), detecting, identifying, and characterizing artificial and natural chiral materials (37), and standoff detection of biological aerosols (38).

Outdoor field-trial experiments have been conducted as well. Specifically, determination of background and target polarization is commonly done in the infrared for both marine scenes (39) and land scenes (40) to reduce background clutter, reject false targets, and generally improve target detection.

In 1992, Ben-Dor (40) explored the difficulties of discriminating weak signals from background clutter in the longwave infrared (LWIR) regime. They determined degree of polarization by introducing a linear polarizer into their imaging system. Background elements such as vegetation, soil, asphalt, concrete and sea surface were measured. They determined that while utilizing a polarizer was useful in detecting dim targets in cluttered background, the contrast was highly dependent on the environment. Negligible polarization came from vegetation, and near negligible polarization from backgrounds such as barren fields, sand and rocks. The strongest polarization signatures were observed when large, relatively flat surfaces such as the sea, roads, and roofs were imaged. It was noted that the polarization was significantly reduced curing cloudy weather vs sunny weather. Bieszczad 2013 (42) discusses determining the polarization state of a scene and the objects in for LWIR object detection, using a polarizer to determine the second and third Stokes parameters.

As shown above, much polarization-related work generally utilizes post-processing algorithms (43) or image processing (44) to remove background clutter. This, however, is not ideal for real-time, short engagement scenarios. This dissertation focuses on material level characterization, which can lead to categorization and discrimination of different systems and signals. The advantages of the polarization approach include utilizing any observed polarization shifts to identify materials under test, extinguishing of non-retroreflected signals, and determining the minimum signal needed to detect change.

Once the properties of the signals are understood it is easier to manipulate them. As an example, there exists a polarization control parallel in radio frequency systems. Converting linear to circular polarization in field-programmable gate arrays (FPGA) was

established by Das 2010 (45) for radio astronomy applications. In this instance, maintaining polarization purity is key. The more direct control over the polarization conversion, the closer one can be to achieving the desired purity level.

In Chun 1997 (46), they explored methods for capturing images of polarization data utilizing the first three Stokes parameters. The polarization-sensitive thermal imaging sensor captured changes in shape and temperature in real time. Simultaneously, Chipman 1997 (47) determined a method for computing diattenuation, retardance, depolarization, and polarizance from the Mueller matrix information.

Another popular method for determining Mueller matrix information is via Mueller matrix imaging polarimetry. Pezzaniti 1995 (48) discusses a Mueller Matrix Imaging Polarimeter (MMIP), which measures polarization properties in both the visible and near-infrared (NIR) regimes. It is used to measure the polarization/polarization scrambling properties of optical elements in a high-spatial-resolution image. It can also be used for measurements in transmission, reflection, retroreflection, and variable-angle scattering. The MMIP has been used for a variety of characterizations including beam splitter cubes (49), scattering surfaces (50), liquid crystal modulators (51), electro-optic PLZT modulators (52), GaAs/AlGa/As waveguide beam splitters (53), as well as polarization signatures of spherical and conical targets (54). DeBoo 2005 (55) studied polarization properties of scattered and diffusely reflected light from man-made gratings, and utilized scattered light polarimetry to measure the Mueller matrices of various materials including a metal box part, nylon plastic material, canvas with paint splotches, sidewalk concrete, glass diffuser, gold-coated glass diffuser, and a screen mesh. Utilizing a Mueller matrix imaging polarimeter, De Boo determined that circular polarization states

generally have more depolarization occurring than do linear states. Liquid crystals are often utilized as variable retarders in Mueller polarimeters (56) - 58).

Corner cube reflector (CCR) polarization relations are discussed in Liu 1997 (59) and more recently in Crabtree 2010 (60), where CCR theoretical and experimental Stokes vector, Jones vector, and Mueller matrix components are examined. The contributions of tilt in samples under test to the Mueller matrix data are also discussed. Bieg (61) showed theoretically via ray tracing and Jones matrices that there occur changes in the polarization upon reflection from a CCR. The output polarization was determined to be dependent on input polarization, wavelength and angle of incidence such that the change can be minimized with reduction of angle between the incident beam and the CCR axis of symmetry. Kalibjian 2004 (62) conducted experiments with a CCR irradiated at normal incidence to show conversions of various polarization states including elliptical to linear, as well as preservation of circular and linear polarizations. Kalibjian 2007 (63) extended the analysis to the case of non-normal incidence.

In Moreno 2003 (64), they analyze changes to linearly polarized light passing through a Dove prism from a Jones calculus perspective. Yun 2009 (65) explores the retardance in three-dimensional polarization ray tracing of a Dove Prism via a Jones calculus perspective.

Effects of various liquid crystal (LC) materials and devices on polarization states of gratings have been shown (66). Herke (67) explored LC precision optical devices where it was found that the polarization state changed more at lower applied voltages (rotation occurs primarily when the applied voltage is near zero). Harris (68) and follow-on research by Anisimov (69) studied reflective liquid crystal optical phased arrays

(LCOPA) at normal and non-normal incidences, and their sensitivity to tilt. In Harris, these effects were categorized into three types: alignment errors, LC director three-dimensionality, and non-normal incidence. Other LC devices and their polarization effects studied previously include spatial light modulators (70). Some studies (68) - 69) were performed in terms of Stokes vectors; for a more detailed analysis of polarization properties, Mueller matrix methods are generally used (62). López-Téllez 2014 (71) detailed the Mueller Matrix for a Glan-Thompson prism, as a representation of a Liquid Crystal Variable Retarder (LCVR), to determine the function of retardance based on voltage.

The LC considered in this dissertation is a Boulder Nonlinear Systems (BNS) liquid crystal polarization grating (LCPG) with liquid crystal (LC) retarder switch, which provides wide angle beam deflection. Anisimov 2008 (69) confirmed that there were polarization issues arising from Liquid Crystal Optical Phased Arrays (LCOPA) utilized for optical beam steering.

In Chapter 2 of this dissertation, the focus is on the aliasing that can occur in sensors, including background information regarding aliasing and the results of analysis performed on various sensors as well as the alias-detecting algorithm are discussed. A theory is presented that simulates the interactions of the signals with the sensor when incident light modulated around or at a harmonic of the frame rate. Verification of the aliasing range on two sensors, one with a fixed frame rate and one with a variable frame rate is shown, as well as the effects of laser-modulation frequency on the sensors. Various frequency modulations are tested against the tracking algorithms of the fixed-frame rate

sensor. The limits of sensors due to aliasing (occurrence of “blind spot” due to frame rate) are discussed, and results of the antialiasing algorithm are presented.

In Chapter 3, background theory regarding polarization and the various vector and matrix representations of polarization are present. This includes the mathematical background of the Stokes Vector, the polarization ellipse, and the Mueller Matrix, as well as discussion of the potential for discrimination capabilities of input signals based on polarization analysis. The novelty of this research lies with the analysis of the data and the equipment used to collect the data.

The Mueller matrix data is collected with The Scatterworks, Inc. Complete Angle Scatter Instrument (CASI) system. This instrument is traditionally used for Bidirectional Reflectance Distribution Function (BRDF) measurements. The version of this system used by the Optics Center at The University of North Carolina at Charlotte (UNCC) utilizes additional software, specifically created for UNCC, to take Mueller Matrix measurements for polarization data collection. From discussions with the vendor and literature searches, UNCC is currently the only group utilizing the CASI system for Mueller matrix polarization data collection and analysis in this manner. This effort has included closely working with the vendor to optimize processes for future work, as well as refining the process for improved analysis. The techniques developed here for laboratory and field-testing purposes can be transitioned and implemented into ongoing efforts and applications. The goal is to optimize the response and effectiveness of sensors. This includes analysis of polarization data from various surfaces to categorize and identify various signals and the groundwork for self-optimizing sensors for future on-the-fly laboratory and field-testing applications.

The dissertation concludes with a discussion in Chapter 4 of the results presented in chapters 2 and 3, continuing into the layout for future experimentation and applications.

CHAPTER 2: ALIASING OF SENSORS

The interaction between the frame rate of the sensor and modulation frequency of the laser is identical to the beat frequency of two tones close in frequency. For visualization purposes, two rectangle functions are utilized – one assigned to the frame rate and the other assigned to the modulation frequency, respectively, of the form:

$$\Pi(t+f) = \begin{cases} 0 & \text{if } \left|t + f_{fr,mf}\right| > 1 \\ w_{fr,\,mf} & \text{if } \left|t + f_{fr,mf}\right| = 1 \\ 1 & \text{if } \left|t + f_{fr,mf}\right| < 1 \end{cases} \qquad [\ 1\ ]$$

Here w_{fr} represents the sensor timing for each frame (akin to on-off keying with "off" represented as 0 and "on" as 1) with the period of the function relating to the frame rate of the sensor, w_{mf} is the pulse width of the QCL, f_{fr}=100 Hz for the frame rate, and f_{mf} is the variable modulation frequency. When the sensor is capturing a frame, it is considered "on" therefore the function is equal to one. When the sensor is not capturing a frame, it is considered "off" and therefore the function is equal to zero. The same is true of the modulation frequency of the laser: when the laser is firing/pulsing, each pulse represents the laser being "on" and the function representing it equals one. When the laser is not firing, between each pulse, the laser is considered off and the rectangle function is equal to zero. The frequency of both the frame rate and the modulation of the laser is represented by the respective periods, f_{fr}, of the rectangle functions. In Figure 1 below, the frame rate (solid red) and modulation frequency (dashed blue) are shown. The frequencies have been scaled by a factor of 1/10 for better visualization. The overlapping (aliasing) areas are highlighted in yellow.

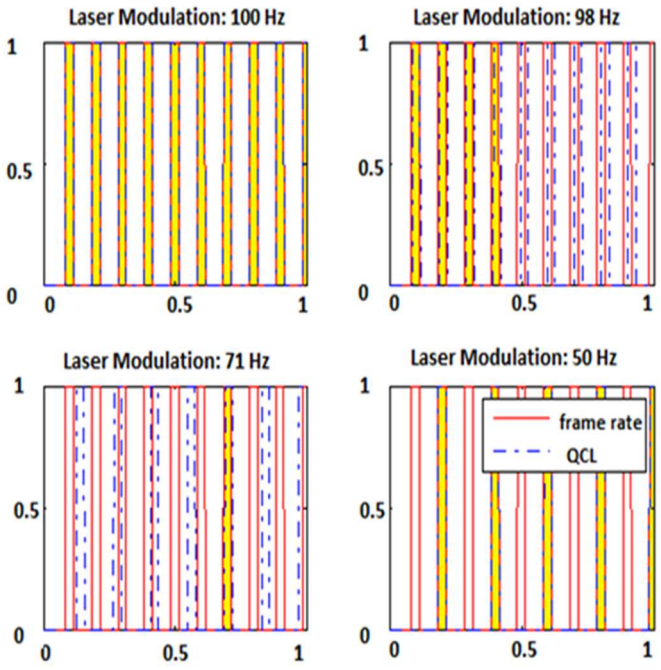

Figure 1: One-second snapshot of the frame rate vs modulation frequency.

As seen in Figure 1 above, aliasing (the indistinguishability of the two signals) occurs when the modulation frequency of the QCL is matched to the frame rate of the sensor. While the period for the frame rate remains the same (100 Hz), the period for the QCL was modulated. Here, f_{mf} = 100, 98, 71, and 50 Hz corresponding respectively to show the situations where the frame rate and modulation frequency are matched, within the ±2 Hz window, an arbitrary frequency, and a subharmonic of the frame rate. When the framerate is 100 Hz and the modulation frequency of the laser is 100 Hz, the system exhibits aliasing, therefore the functions in Figure 1 are exactly overlaid. When the modulation frequency is within the 10 Hz window, there is some overlap and the functions are close enough that they are still mostly indistinguishable, as seen in Figure 1 with the frequency of 98 Hz. At an arbitrary modulation frequency, here in Figure 1

shown as 71 Hz, the two signals are distinct and easily separated. However, at a subharmonic of the framerate, here 50 Hz, the signals are once again aliased.

There is also a phasing effect between the laser pulse frequency and camera framerate. As the modulation frequency approaches the sensor frame rate, it increases the probability of the laser pulse being out of phase with the sensor frame rate. The laser pulse waveform is said to be out of phase with the frame driving waveform. This can also be said to occur when the laser pulse captures are out of sync with the framerate capture. This is similarly valid at the harmonics. If the integration time of the sensor and the modulating laser are 180 degrees out of phase, it negates any effect the laser has on the sensor. Since the laser and sensor are triggered asynchronously, and as a result are never perfectly in sync, small drifts in frequency and timing are always present. However, the sensor and laser may be brought back into sync over a period of several seconds or minutes. It is not desirable to have them sync unless it is synced to the "on" portion of the frame capture, otherwise, the camera image will not record any of the incident energy on an image.

To characterize the laser's effect on the sensor when modulated at various frequencies, the difference in intensity from frame to frame difference was measured. A mathematical representation of this value was developed at Aberdeen Proving Ground, labeled FINC (Flicker, Instantaneous Normalized Contrast) (72). Flicker is a modulation of the luminous flux of a light source, instantaneous is the difference of one frame intensity subtracted from the other, normalized frame-to-frame, and the two objects are the consecutive frames in question. This produces a value which correlates contrast with

the constant framerate of the sensor as the framerate and the laser frequency are varied. Corresponding to frame number n, FINC is defined as:

$$FINC_n = \frac{(I_n - I_{n-1})}{I_n} \quad [2]$$

$$FINC_{MAX} = MAX(FINC_n) \quad [3]$$

$$FINC_{MEAN} = \frac{\Sigma FINC_n}{I_{total}} \quad [4]$$

The FINC number dips to zero as aliasing is observed. The minimums in the FINC number are seen occur at integral harmonic overtones and halftones of the frame rate, also referred to here as the "fundamental frequency" (f_0) as well as at subharmonics of the fundamental frequency. For example, a frequency of 95 Hz would not have a strong effect, but 98 Hz is closer to the fundamental so the "beating" is observed at 100 -98 Hz, the closest to minimum. The minimum here occurs due to both the sampled energy from the laser signal lining up asynchronously with the portion of the camera frame integration period, yet not lining up perfectly with on or off camera integration periods. This minimum reemerges at the harmonics and subharmonics. Therefore, while effects are most noticeable/effective at the exact fundamental frequency, there are still observable effects at the harmonics and subharmonics. The purpose of this portion of the research is to investigate the strength of the various harmonics and subharmonics away from the fundamental frequency. From this, we see the peaks are observed at f_0, f_0+nf_0, $f_0+n/2f_0$, $f_0+n/3f_0$, etc. and the subharmonics are f_0/n, etc., where n is an integer. However, this predictive pattern may be disrupted due to the relationship between the laser pulse and frame rate breaking down when overlap occurs such that one or the other appears continuously "on" or "off" (73).

Testing continued with frequencies within the vicinity of the 100 Hz frame rate. It was observed that a ±10 Hz window on either side of the frame rate frequency interfered the most with the tracking algorithm. The effect of the frequencies outside the 100 Hz ± 10 Hz range had sporadic effects on the sensor's ability to see the laser. To determine the consequences of the laser modulation frequency on the sensor, the QCL was modulated at a range of frequencies centered about the sensor frame rate (100 Hz). This window and the harmonics are shown in Figure 2.

One method of analyzing the aliasing effects on the fixed frame rate sensors utilized the internal image processing of the sensor, which predicts location changes when the laser is within a frame. Figure 3 shows the azimuth and elevation angles of the "line of sight" of the sensor, with respect to the center of the field of view, over the period which the sensor is on. The azimuth and elevation angles are with respect to the center of the sensor's field of view. We see the sensor's image processing software can follow the cyclic pattern of an object projected on the scene projector, until it is diverted by the appearance of the laser spot around 450-475 frames. Figure 4 shows the same scene but this time as a function of which pixels the image processing software is observing. The predicted pixel location of the object, as output from the sensor's image processing software, is used as a second method of cataloging where the sensor is "looking". Again, when the laser is introduced, the location the sensor is "looking" at changes – the cyclical tracking pattern is disrupted, and the tracking becomes erratic and non-cyclical.

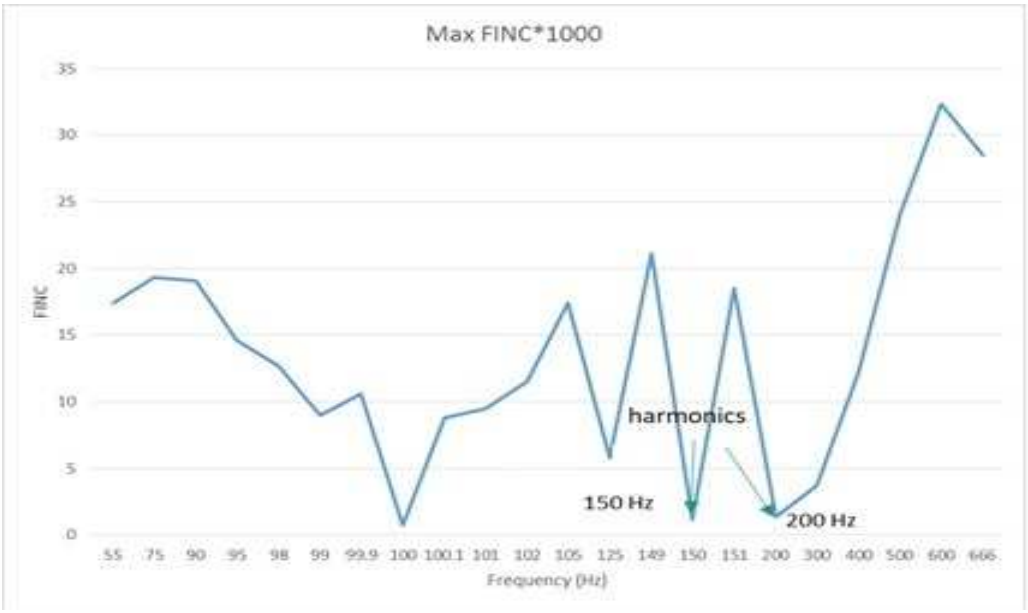

Figure 2: FINC of fixed frame rate sensor

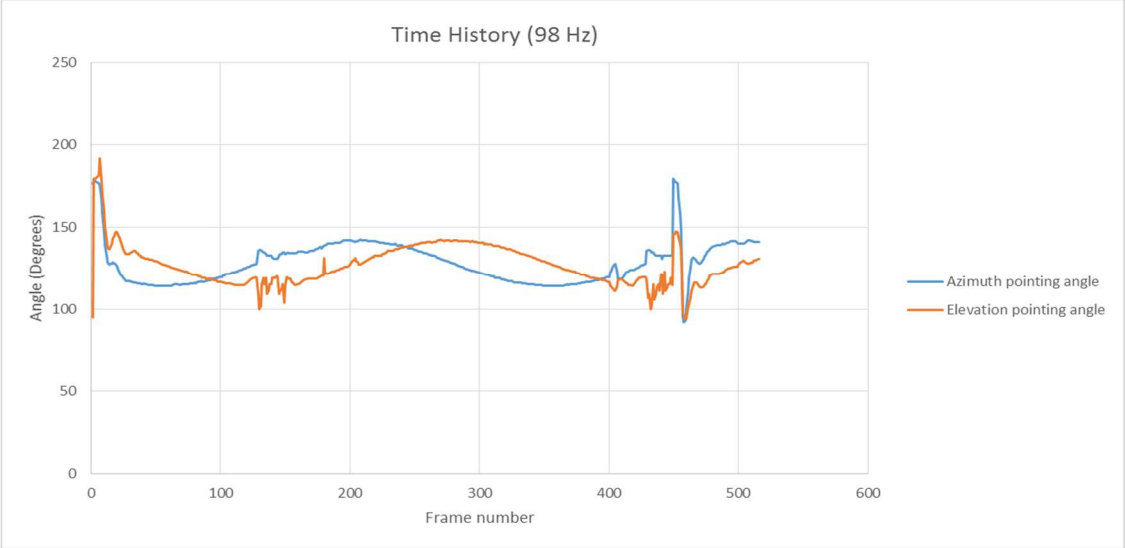

Figure 3: Time history of the fixed frame rate sensor at 98Hz laser modulation

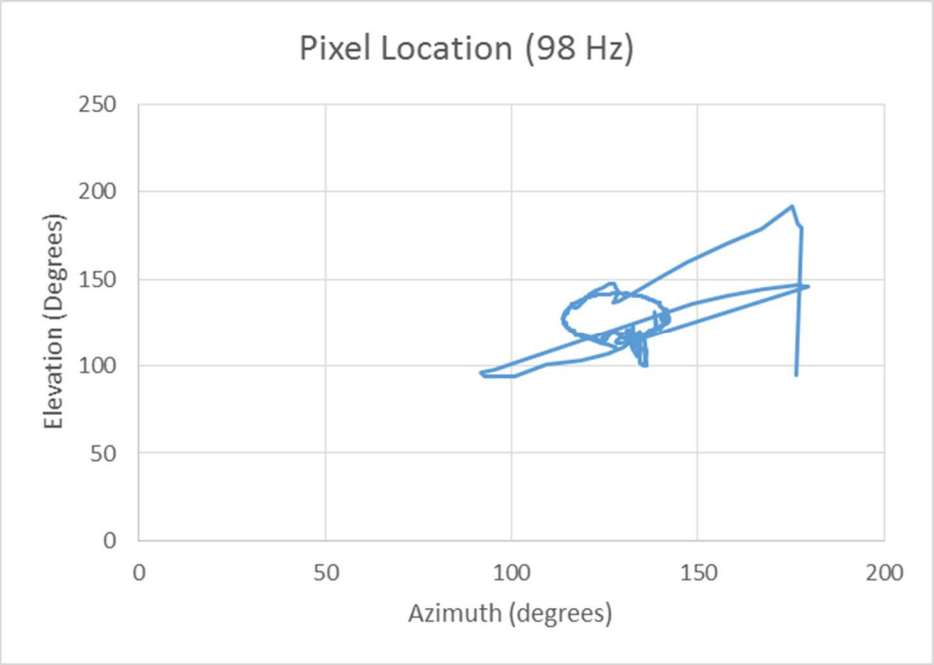

Figure 4: Pixel location of the laser in the fixed frame rate sensors

When the frame rate of the sensor is fixed, and it is necessary to change the frequency of the laser signal via trial and error to successfully test a system. The ideal sensor would be able to autonomously adjust itself when encountering a signal that is modulated at its frame rate to avoid the beat frequencies encountered in the previously shown results. To demonstrate this point, an algorithm was developed in MATLAB to autonomously adjust the frame rate when the input signal frequency matched the frame rate of the sensor. For visual verification purposes an optical chopper was used, with its frequency set to match the frame rate. The QCL modulation frequency remained unchanged for this test. As seen in Figure 5 and Figure 6 below, when the frame rate matched the signal frequency (blue in Figure 5, red in Figure 6), the algorithm adjusted the sensor's frame rate (green in Figure 5, Figure 6). The algorithm accounts for the harmonics of the original frequency, so there will be no accidental aliasing. When the

intensity of consecutive frames is within a certain threshold, the algorithm changes the FLIR frame rate and takes the data again. The end goal is to observe the increase in irradiance fluctuations in the camera's processed image while the irradiance on camera remains the same. In Figure 6, both the aliased and non-aliased cases show drifting.

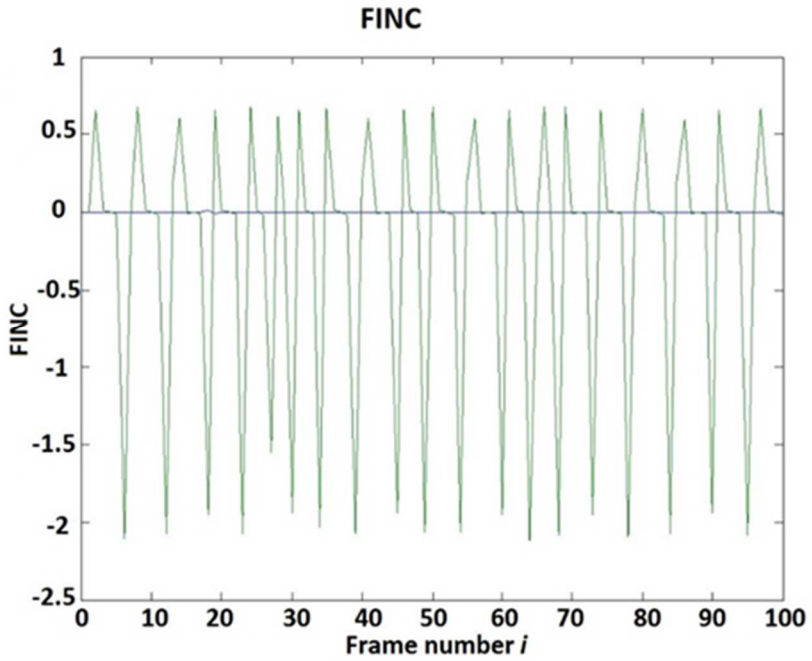

Figure 5: FINC per frame, aliased (blue) vs not aliased (green)

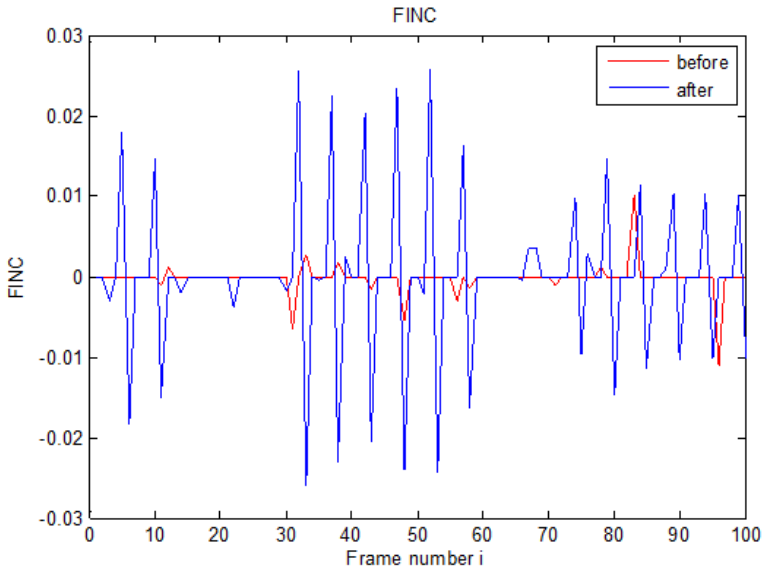

Figure 6: FINC of FLIR at 125 Hz when aliased
before (red) and not aliased after (blue)

As shown in Figure 6 above, the drifting occurs as shown by the disparity of the amplitude of each pulse packet. The algorithm considers the harmonics and subharmonics of the original rate to avoid them. A variety of test cases were run, ranging from 50 Hz to 800 Hz. During a few runs, there were offsets noticed in the laser and the sensor due to unmatched trigger times as shown in Figure 7 below. This drifting due to unmatched time syncing is evident in the "before" from two aspects. The first is the disparity in FINC amplitude between the first set of frames and the second set of frames. The second is the disparity in the number of frames where the FINC is non-zero. In practical applications, such as a field environment, this asynchronous scenario is entirely plausible.

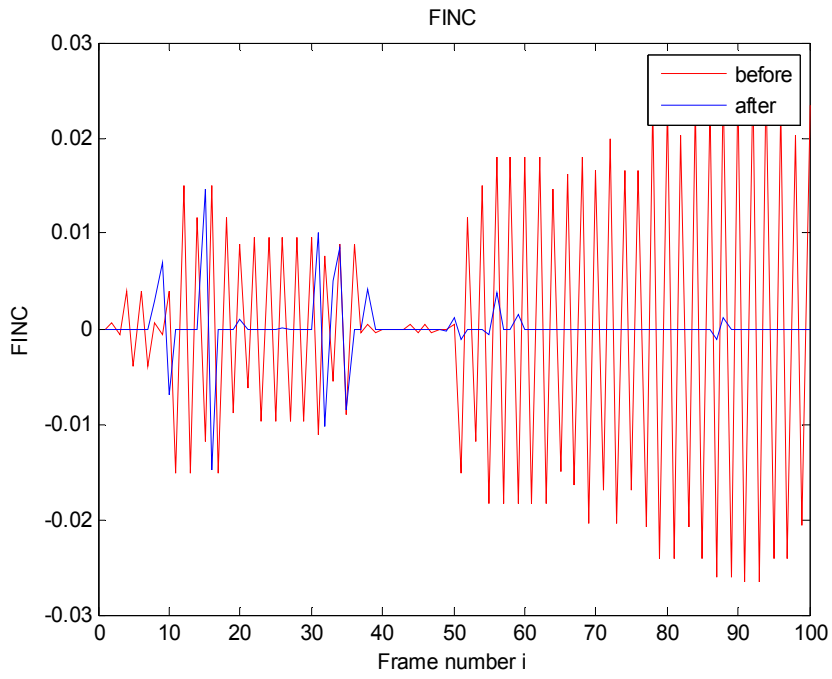

Figure 7: FINC of FLIR at 125 Hz when not aliased before (red) and aliased after (blue)

From these experiments, the advantages of an adjustable frame rate sensor over a fixed frame-rate sensor are evident, based on the sensor's potential ability to adapt to situations where aliasing can occur. This advantage is greatly increased with the use of an aliasing detection algorithm. Future improvements to the algorithm will require compensation for the drifting discovered during these experiments.

CHAPTER 3: POLARIZATION & THE MUELLER MATRIX

Polarization is defined as the orientation of the electric field, $\vec{E}$, for a transverse electromagnetic wave (transverse electromagnetic waves are waves in which the electric and magnetic fields oscillate perpendicularly to the direction of propagation). Polarized light comes in four forms of polarization: unpolarized (also known as randomly polarized), linear (as known as plane polarization, where the $\vec{E}$ field is confined to a plane along the direction of propagation for either x, y, or a combination), circular (the $\vec{E}$ field in x and y are equal), and elliptical (the $\vec{E}$ field in x and y are unequal).

Table 1: Electric field orientation of the four polarization types

Polarization Types	**$\vec{E}$ field orientation**
Unpolarized/randomly	Multiple directions/planes, may be asymmetric
Linear/plane	x-plane if horizontal (0°), y-plane if vertical (90°), xy-plane for angles other than 0° and 90°
Circular	x and y are equal
Elliptical	x and y are unequal

Changes in the polarization of a waves can be a result of absorption (diattenuation/dichroism), reflection, scattering (depolarization), or birefringence (retardance).

The various components describing polarization are based on the polarization ellipse, Figure 8, which accounts for amplitudes in x and y and phase components. Every polarizing element causes a change in one of these domains. Types of polarizing

elements include polarizers (amplitude change), retarder/phase shifter (phase change) or rotator (phase change) depending on the element, m_{aa} components of the Mueller matrix. For example, a linear polarizer is characterized by the absorption coefficients while waveplates/retarders/phase shifters by the phase shift. Rotators are characterized by the angle of rotation. Table 2 shows these variables and their ranges. Ellipticity angle and orientation angle are determined by the Stokes parameters, detailed in the next section.

Table 2: Variables of Stokes Vector, Jones and Mueller Matrices.

Characteristic	**Equation/Representation**	**Range**
absorption coefficients	p_x, p_y	$0 \leq p_x, p_y \leq 1$
angle of rotation	θ	$0° \leq \theta \leq 360°$
ellipticity angle	$\chi = \frac{1}{2} tan^{-1}\left(\frac{S_2}{S_1}\right)$	$-\pi/4 \leq \chi \leq \pi/4$
orientation angle	$\psi = \frac{1}{2} sin^{-1}\left(\frac{S_3}{S_0}\right)$	$0 \leq \psi \leq \pi$
total phase shift	$\varphi = \varphi_x - \varphi_y$	$0 \leq \varphi \leq \pi$

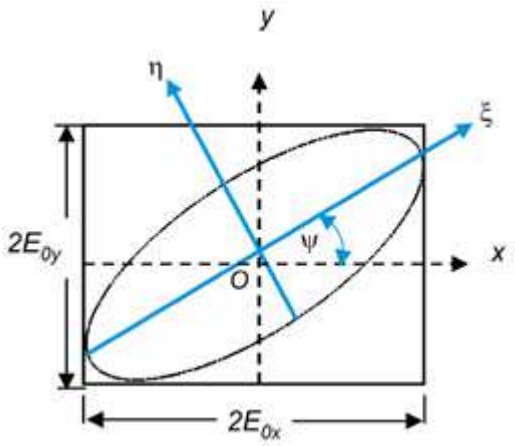

Figure 8: The polarization ellipse

3.1 Stokes Vector

There various ways to represent polarization states, including Stokes vector, and Mueller matrix. First, in matrix representation, the input beam is defined by a Stokes

vector S and the output beam by S'. The Stokes vectors, shown in the equation below, provide information on the total irradiance of the beam (S_0), horizontal/vertical orientation of the $\vec{E}$ field (S_1), ± 45° orientation of the $\vec{E}$ field (S_2), and the left/right handedness of any circular or elliptical polarization present (S_3).

$$S = \begin{bmatrix} S_0 \\ S_1 \\ S_2 \\ S_3 \end{bmatrix} \quad [5]$$

where S_0, S_1, S_2, and S_3 are the stokes parameters defined by the following set of equations. Recall, χ and ψ are ellipticity angle and orientation angle respectively.

$$S_0 = I \quad [6]$$

$$S_1 = S_0 \cos(2\chi)\cos(2\psi) \quad [7]$$

$$S_2 = S_0 \cos(2\chi)\sin(2\psi) \quad [8]$$

$$S_3 = S_0 \sin(2\chi) \quad [9]$$

The first Stokes parameter, S_0, shown above is defined as the total intensity I of the beam. The value of this parameter ranges from 0 to 1. Since the value is usually normalized, the standard value is 1.

The second Stokes parameter, S_1, is the amount of linear horizontal or vertical polarization in the beam. The $I = \pm 1$ cases describe full transmission in one direction (either horizontal or vertical, respectively), and the $I=0$ case would indicate no transmission in either direction.

The third Stokes parameter, S_2, in is defined as the amount of ±45° polarization in the beam. Similar to the second Stokes parameter, the $I = \pm 1$ cases describe full

transmission in one direction (here either +45° or -45°, respectively), and *I=0* denotes no transmission in either direction.

The fourth and final Stokes parameter, S_3, describes the amount of right or left circular polarization in the beam. Again, he $I = \pm 1$ cases describe full transmission in one direction (right circular or left circular, respectively), and the $I=0$ case as no transmission in either direction.

3.2 Mueller Matrix

The method for representing the change in polarization state that occurs from incident beam S to outgoing beam S' is via the Mueller matrix. This is a transformation matrix that acts on an incoming beam of light (denoted by the Stokes vector S) to change it to the output beam (denoted by Stokes vector S'):

$$\begin{bmatrix} S'_0 \\ S'_1 \\ S'_2 \\ S'_3 \end{bmatrix} = \begin{bmatrix} m_{00} & m_{01} & m_{02} & m_{03} \\ m_{10} & m_{11} & m_{12} & m_{13} \\ m_{20} & m_{21} & m_{22} & m_{23} \\ m_{30} & m_{31} & m_{32} & m_{33} \end{bmatrix} \begin{bmatrix} S_0 \\ S_1 \\ S_2 \\ S_3 \end{bmatrix} \qquad [\ 10\ ]$$

where $-1 \leq m_{aa} < 1$ and a = [0 1 2 3].

Isotropic materials have Mueller matrices that are solely diagonal matrices, all non-diagonal elements are zero. For elements that do not cause any polarization change, the Mueller matrix equation is a diagonal matrix shown below. Mueller matrix for an absorber and depolarizer (an optic which outputs randomly polarized light, the opposite of a polarizer) are shown in the equations below. The m_{00} component is traditionally equal to one, as it is the normalization component for the matrix. Components m_{11}, m_{22}, and m_{33} are associated with depolarization.

$$M_{non-pol} = \begin{bmatrix} 1 & 0 & 0 & 0 \\ 0 & 1 & 0 & 0 \\ 0 & 0 & 1 & 0 \\ 0 & 0 & 0 & 1 \end{bmatrix} \quad [11]$$

$$M_{absorb} = \begin{bmatrix} m & 0 & 0 & 0 \\ 0 & m & 0 & 0 \\ 0 & 0 & m & 0 \\ 0 & 0 & 0 & m \end{bmatrix} \quad [12]$$

$$M_{depol} = \begin{bmatrix} 1 & 0 & 0 & 0 \\ 0 & m & 0 & 0 \\ 0 & 0 & m & 0 \\ 0 & 0 & 0 & m \end{bmatrix} \quad [13]$$

The off-diagonal components of the Mueller matrix describe the effects of diattenuation (amplitude change), or retardance (phase change) on the $\vec{E}$ field of a wave incident on a surface. The terms "diattenuation" and "retardance" are defined in *Handbook of Optics, Volume I* (74) as the intensity of the exiting light relative to the input polarization, and the phase change based on polarization, respectively. Examples of each are a linear polarizer (diattenuator), and a quarter waveplate (QWP) (retarder), respectively. The equation below denotes the off-diagonal elements of the Mueller matrix, and Table 3 correlates these off-diagonal Mueller matrix components to their polarization properties.

$$M = \begin{bmatrix} 0 & a & b & c \\ a & 0 & -d & -e \\ b & d & 0 & -f \\ c & e & f & 0 \end{bmatrix} \quad [14]$$

Table 3: Properties of the off-diagonal Mueller matrix components

Mueller Matrix Components	**Properties**	**Stokes Parameter Equivalent**	**Example Polarizer**
a (m_{01}, m_{10})	linear diattenuation oriented at 0° or 90°	S_2	Liner polarizer/diattenuator (horizontal or vertical transmission axis)
b (m_{02}, m_{20})	linear diattenuation oriented at 45° or 135°	S_3	Linear polarizer/diattenuator (+45° or -45° transmission axis), rotates polarizer/diattenuator
c (m_{03}, m_{30})	circular diattenuation	S_4	Circular polarizer (right-handed or left-handed)
d (m_{12}, m_{21})	linear retardance oriented at 0° or 90°	N/A	Rotator (vertical or horizontal transmission axis), rotated polarizer/diattenuator
e (m_{13}, m_{31})	linear retardance oriented at 45° or 135°	N/A	Rotator (+45° or -45° transmission axis), rotated retarder/waveplate
f (m_{32}, m_{23})	circular retardance	N/A	Retarder/waveplate

Depolarization and inhomogeneities occur when there are asymmetries in either a, b, c or symmetry in d, e, f (74). Note, here the nomenclature for symmetry and asymmetry refers to the sign convention as well as the magnitude with symmetry referring to matching signs and asymmetry opposite signs. For example, ideal diattenuators are symmetric, having the equal values for a, b, and c because they attenuate uniformly and ideal retarders are asymmetric, with opposite values for d, e, and f because they retard aspects of the electric field non-uniformly, therefore a reversal of these results indicates imperfection or asymmetry in the subject under test (SUT). As mentioned above, the range of the Mueller values are from -1 to +1. The transmissions axis of a linear polarizer

is indicated by +1 for at 0°, 45° and -1 for 90°, 135° (-45° in some nomenclature), respectively.

These changes in diattenuation and retardance are shown in the Mueller matrices for various polarizing components shown below. For linear diattenuators (more commonly referred to as linear polarizers) the Mueller matrix is given below:

$$M_{LP}(p_x, p_y) = \begin{bmatrix} {p_x}^2 + {p_y}^2 & {p_x}^2 - {p_y}^2 & 0 & 0 \\ {p_x}^2 - {p_y}^2 & {p_x}^2 + {p_y}^2 & 0 & 0 \\ 0 & 0 & 2p_x p_y & 0 \\ 0 & 0 & 0 & 2p_x p_y \end{bmatrix} \quad [15]$$

From this we see the off-diagonal Mueller matrix components of a linear polarizer detail linear diattenuation oriented at 0° or 90°.The Mueller matrix for horizontal polarizers and vertical polarizers respectively shown below, where $p_x = 1$, $p_y = 0$, and, where $p_x = 0$, $p_y = 1$. We see the necessary symmetry in a (m_{01}, m_{10}) for these polarizers to to be ideal. For a neutral density (ND) filter, $p_x = p_y = p$ the Mueller matrix reduces to that for an absorber, mentioned above.

$$M_{HP} = \begin{bmatrix} 1 & 1 & 0 & 0 \\ 1 & 1 & 0 & 0 \\ 0 & 0 & 0 & 0 \\ 0 & 0 & 0 & 0 \end{bmatrix} \quad [16]$$

$$M_{VP} = \begin{bmatrix} 1 & -1 & 0 & 0 \\ -1 & 1 & 0 & 0 \\ 0 & 0 & 0 & 0 \\ 0 & 0 & 0 & 0 \end{bmatrix} \quad [17]$$

$$M_{\substack{ND \\ filter}} = p^2 \begin{bmatrix} 1 & 0 & 0 & 0 \\ 0 & 1 & 0 & 0 \\ 0 & 0 & 1 & 0 \\ 0 & 0 & 0 & 1 \end{bmatrix} \quad [18]$$

Recall, the Mueller matrix elements m_{01} and m_{10} correspond to linear diattenuation oriented at 0° or 90°, as is expected for horizontal and vertical linear polarizers,

respectively. Similarly, for the ±45° linear Mueller matrices below, the m_{02} and m_{20} are denote linear diattenuation oriented at 45° and 135°, respectively.

$$M_{+45^\circ} = \begin{bmatrix} 1 & 0 & 1 & 0 \\ 0 & 0 & 0 & 0 \\ 1 & 0 & 1 & 0 \\ 0 & 0 & 0 & 0 \end{bmatrix} \quad [19]$$

$$M_{-45^\circ} = \begin{bmatrix} 1 & 0 & -1 & 0 \\ 0 & 0 & 0 & 0 \\ -1 & 0 & -1 & 0 \\ 0 & 0 & 0 & 0 \end{bmatrix} \quad [20]$$

For a rotated polarizer, the m_{01}, m_{10}, m_{02}, m_{12}, m_{20}, m_{21}, and m_{22} components of the Mueller matrix are all affected by the rotation where θ is the angle of the rotation. Recall, linear diattenuation oriented at 45° or 135° occurs in m_{02} and m_{20}, linear retardance oriented at 0° or 90° in m_{12} and m_{21}. Here, θ = 0°, ±45°, and 90° are defined for the special cases of linear polarizers mentioned above: horizontal, ±45°, and vertical, respectively.

$$M_{\substack{ideal \\ rot.\ LP.}}(\theta) = \begin{bmatrix} 1 & cos2\theta & sin2\theta & 0 \\ cos2\theta & \cos^2 2\theta & sin2\theta cos2\theta & 0 \\ sin2\theta & sin2\theta cos2\theta & \sin^2 2\theta & 0 \\ 0 & 0 & 0 & 0 \end{bmatrix} \quad [21]$$

As shown in the equation above, an ideal linear polarizer rotated at angle θ has components denoting linear diattenuation m_{01}, m_{10} and m_{02}, m_{20}, as well as linear retardance in m_{12} and m_{21}. Components m_{11} and m_{22} represents depolarization. For retarders, the general form of the Mueller matrix is shown in below. Here, the relevant components, m_{32} and m_{23}, are subject to circular retardance, which is expected of a retarder. The off-diagonal Mueller matrix components here indicate the presence of circular retardance. Recall, the diagonal components represent depolarization.

$$M_{WP}(\varphi) = \begin{bmatrix} 1 & 0 & 0 & 0 \\ 0 & 1 & 0 & 0 \\ 0 & 0 & cos\varphi & -sin\varphi \\ 0 & 0 & sin\varphi & cos\varphi \end{bmatrix} \quad [\ 22\ ]$$

Here, φ is the total phase shift and elements $m_{22} = m_{33} = \cos\varphi$, $m_{32} = \sin\varphi$ and $m_{23} = -m_{32} = -\sin\varphi$, respectively. The effect a half wave plate has on linearly polarized light is to rotate the polarization vector by an angle of 2θ. The polarization vector of the exiting beam is rotated through an angle 2θ (for elliptically polarized light, the handedness of the input light is inverted).

An example of this is a halfwave plate, which causes a phase shift of π (or 180°). This is similar to a mirror which causes a phase change of half a wavelength upon reflection. We see for these two components there is no circular retardation which is generally associated with waveplates.

$$M_{HWP}(\varphi = \pi) = \begin{bmatrix} 1 & 0 & 0 & 0 \\ 0 & 1 & 0 & 0 \\ 0 & 0 & -1 & 0 \\ 0 & 0 & 0 & -1 \end{bmatrix} \quad [\ 23\ ]$$

Another example is that of a quarter-wave plate, which converts linear polarization or circular polarization, and vice versa. The expected circular retardance is present in this matrix.

$$M_{QWP}\left(\varphi = \frac{\pi}{2}\right) = \begin{bmatrix} 1 & 0 & 0 & 0 \\ 0 & 1 & 0 & 0 \\ 0 & 0 & 0 & \pm 1 \\ 0 & 0 & \mp 1 & 0 \end{bmatrix} \quad [\ 24\ ]$$

The Mueller matrices for an ideal left-handed circular polarizer and an ideal right-handed circular polarizer are shown below.

$$M_{LHCP} = \begin{bmatrix} 1 & 0 & 0 & -1 \\ 0 & 0 & 0 & 0 \\ 0 & 0 & 0 & 0 \\ -1 & 0 & 0 & 1 \end{bmatrix} \quad [25]$$

$$M_{RHCP} = \begin{bmatrix} 1 & 0 & 0 & 1 \\ 0 & 0 & 0 & 0 \\ 0 & 0 & 0 & 0 \\ 1 & 0 & 0 & 1 \end{bmatrix} \quad [26]$$

The Mueller matrix of a rotated waveplate has the circular retardance occurring in components m_{32} and m_{23} as it occurs in a non-rotated waveplate, as well as m_{12} and m_{21} affected by linear retardance oriented at 0° or 90° and linear retardance oriented at 45° or 135° in m_{13} and m_{31}.

$$M_{\substack{rot. \\ ret.}}(\varphi, \theta) = \begin{bmatrix} 1 & 0 & 0 & 0 \\ 0 & \cos^2 2\theta + \cos\varphi \sin^2 2\theta & (1-\cos\varphi) sin2\theta cos2\theta & -\sin\varphi \sin 2\theta \\ 0 & (1-\cos\varphi) sin2\theta cos2\theta & \sin^2 2\theta + \cos\varphi \cos^2 2\theta & \sin\varphi \cos 2\theta \\ 0 & \sin\varphi \sin 2\theta & -\sin\varphi \cos 2\theta & \cos\varphi \end{bmatrix} \quad [27]$$

For a rotated halfwave plate, φ = 180° this reduces to

$$M_{\substack{rot. \\ HWP}}(180°, \theta) = \begin{bmatrix} 1 & 0 & 0 & 0 \\ 0 & cos\,4\theta & sin4\theta & 0 \\ 0 & sin4\theta & \cos 4\theta & 0 \\ 0 & 0 & 0 & -1 \end{bmatrix} \quad [28]$$

The general Mueller matrix form for a rotator is shown below. The m_{12} and m_{21} components are affected by linear retardance oriented at 0° or 90°, dependent upon the angle of rotation.

$$M_R(\theta) = \begin{bmatrix} 1 & 0 & 0 & 0 \\ 0 & cos2\theta & sin2\theta & 0 \\ 0 & -sin2\theta & cos2\theta & 0 \\ 0 & 0 & 0 & 1 \end{bmatrix} \quad [29]$$

3.3 Reflection and Transmission

When discussing reflection and transmission, the coordinate system is often discussed in terms of the plane of incidence. The commonly utilized terms are parallel-polarization (p-polarization) where the electric field is polarized parallel to the plane of incidence and senkrecht-polarization (s-polarization, senkrecht is German for perpendicular) where the electric field is polarized perpendicular to the plane of incidence.

3.4 Experimental setup

The Mueller matrix data was collected with a Complete Angle Scatter Instrument (CASI) system manufactured by The Scatter Works, Inc. This instrument is traditionally used for Bidirectional Reflectance Distribution Function (BRDF) measurements and this version has additional options for polarization control, with components at the transmitter and receiver which allow Mueller matrix measurements to be made as a function of angle of incidence. This system utilizes lasers as “non-contact probe” radiation sources to measure angle-resolved scattered light. It consists of a moving mount stage which allows for movement in X, and Y and rotation with incident angles up to 85° from surface normal. Both reflective and transmissive scatter measurements can be taken through specular beam and at high scatter angles. The laser wavelength capabilities are 0.633, 1.06, 3.39, and 10.6 um. Figure 9 below shows the CASI setup used in the laboratory at UNC Charlotte.

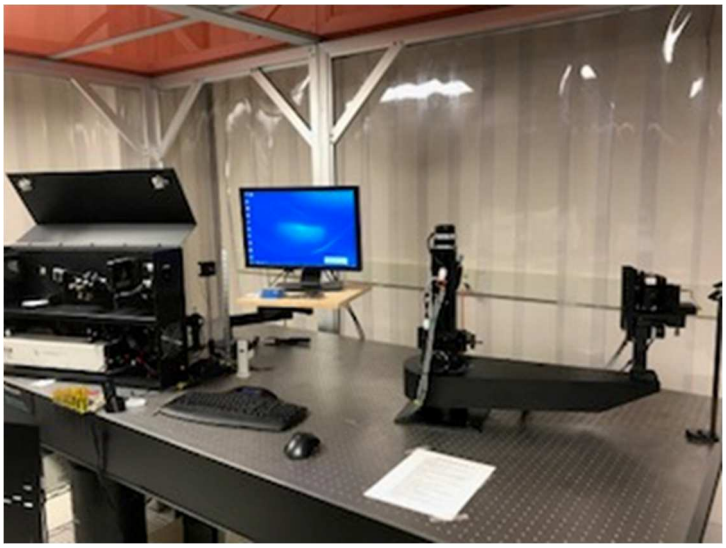

Figure 9: Photograph of CASI setup

The following figures, Figure 10 through Figure 16, come from the CASI Hardware Manual (75) and the CASI User Manual (76). An overhead layout of the CASI system is shown in Figure 10. Figure 11 displays a block diagram of the entire CASI system. Figure 12 and Figure 13 show the layout of the source box and receiver configurations, respectively, with Table 4 presenting the component labels.

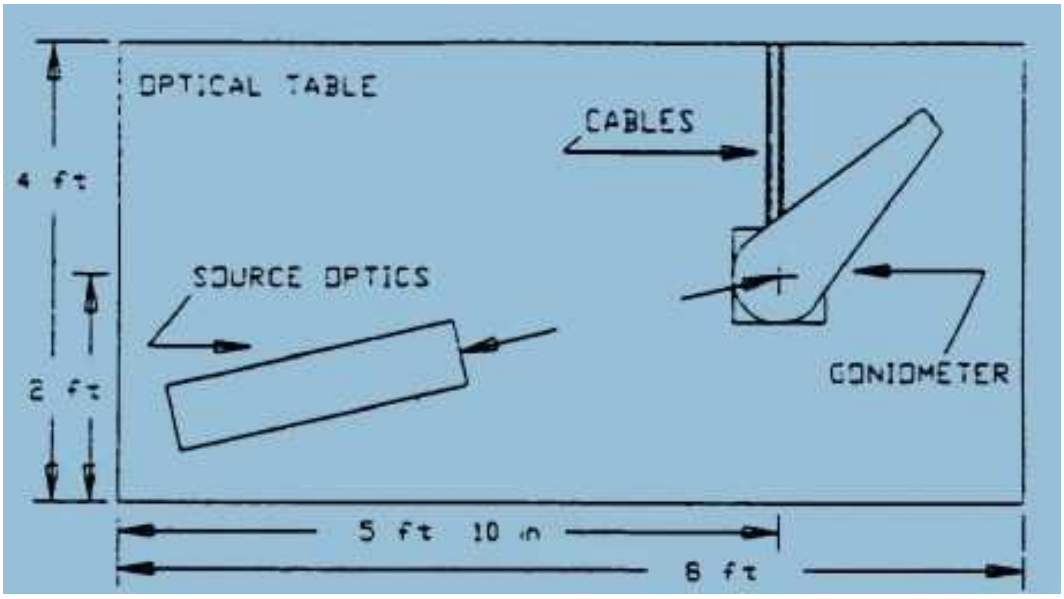

Figure 10: Overhead layout of CASI setup from the user manual

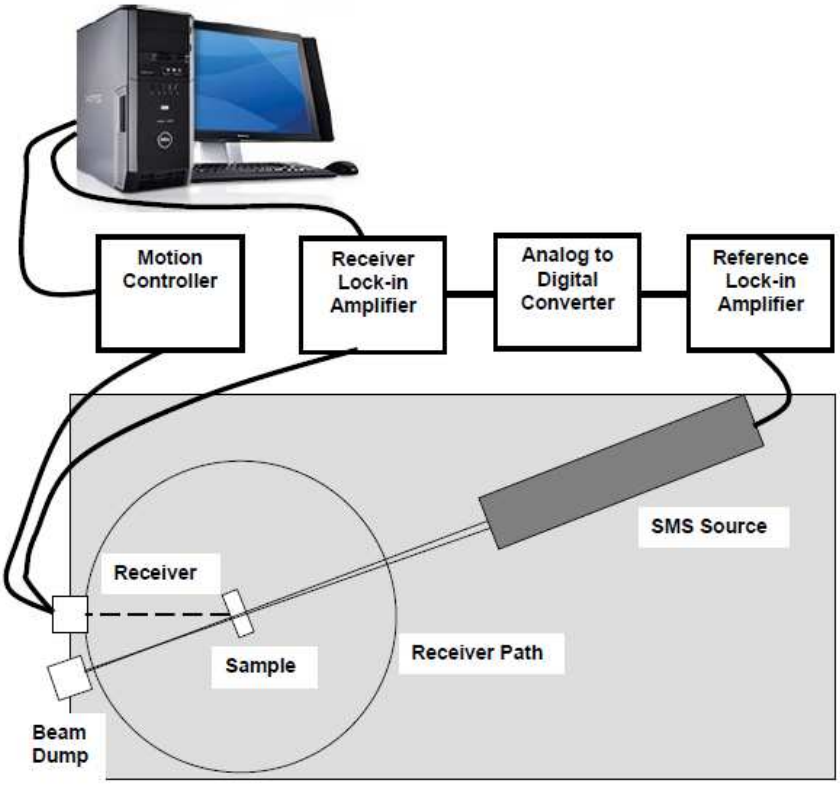

Figure 11: Block diagram of CASI

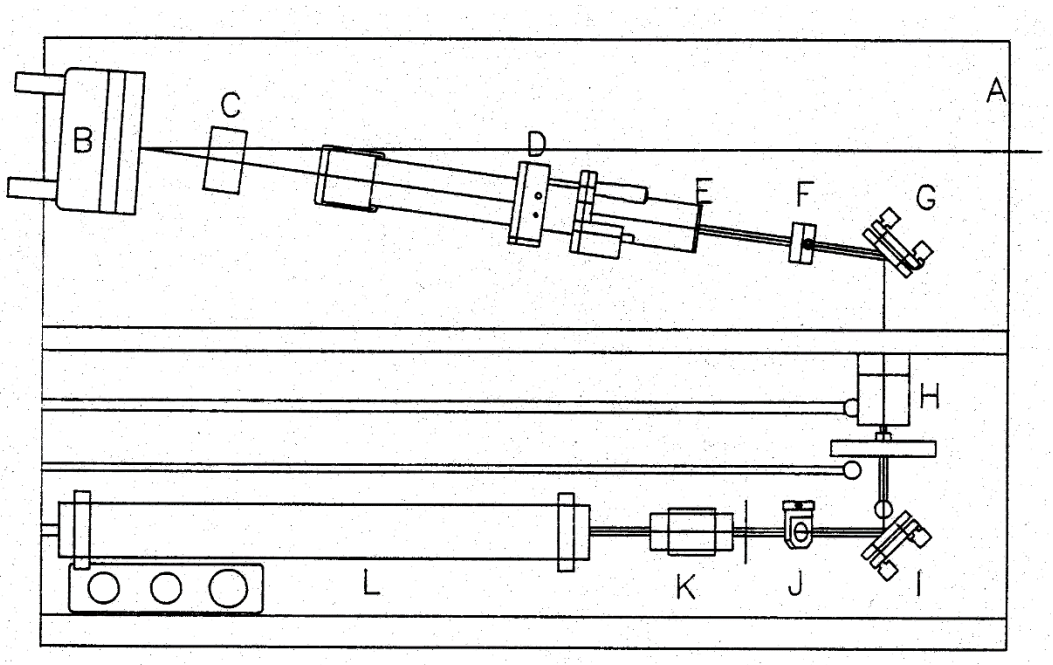

Figure 12: General layout of CASI source box for one source laser (75)

Table 4: Components of CASI source box

Letter Designation	Component	Distance to next element (in)
A	large anodized aluminum plate	26.75
B	Main focusing mirror	25.2
C	Alignment iris 1 (of 2)	10.5
D	Spatial Filter	4
E	Focusing stage	5.2
F	Alignment iris 2 (of 2)	5
G	Turning mirror 1 of 2	2.5
H	Filter Wheel	6
I	Turning mirror 2 of 2	2
J	Reference Detector	2
K	Chopper	3
L	Visible HeNe	N/A

The large anodized aluminum plate (Component A) is used to hold all the optical components. The main focusing mirror, component B, is in the upper half of the Optical Source enclosure. Component C is one of two alignment irises, used to align the laser beam. This ensure that the beam hits the center of the main focusing mirror. The spatial filter, component D, consists of a microscope objective and a pinhole. Component E is the focusing stage. Two turning mirrors (G and I), are used to move the laser beam in the

two alignment irises C and F. Component H is the filter wheel, and component J is a reference detector for measuring the source laser power. It consists of a beam splitter, diffuser and detector element. The chopper, component K, along with the reference detector and the lock-in amplifier is used to remove system noise. L is the HeNe laser and M is the second laser (IR at 10.6um), and the shutters to block each are P and Q, respectively. Turning mirror N is used to bring the laser (M) to the beam combiner (S). A small port (T) is used during the optical alignment of the system described in the next section.

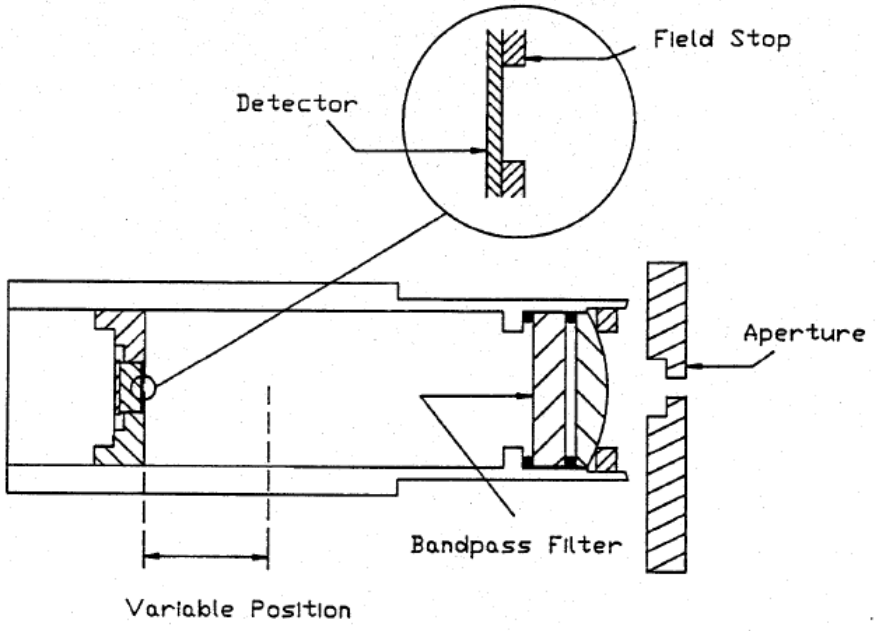

Figure 13: Schematic of the CASI receiver (75)

The receiver end of the system, Figure 13, consists of an aperture, a lens, a bandpass filter, a field stop and the detector element (for 0.633 and 1.06 um it is an Si detector). The receiver has 4 apertures that can adjust to 8 different sizes: 160, 300, 1100,

1600, 2500, 4000, 10000, and 14000 um (note, all are circular apertures except 1600, which is a slit).

3.5 System Coordinates

A coordinate system frequency used when discussing scatter is defined by Nicodemus et. al (77), utilizing a sample based spherical coordinate system. Here, x and y lie in the same plane and the z-direction is normal to the sample. Figure 14 shows the scatter coordinate systems from the sample utilized by Nicodemus, as shown in the scatterometer user manual (76).

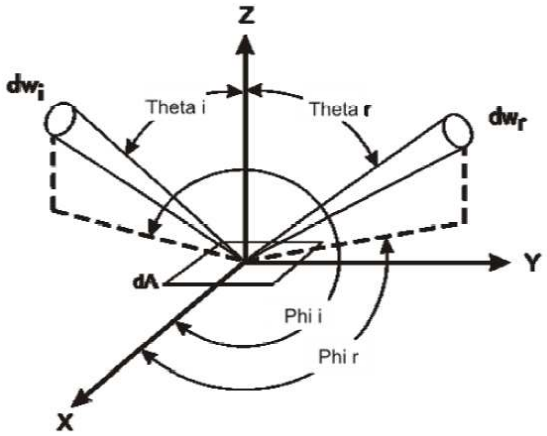

Figure 14: Scatter coordinate system from the sample (76)

The scatterometer axes are defined such that measurements are specified by the location of the illuminated spot on the sample. In other words, the coordinate system is defined as the sample viewed from the source as a positive x-y-z right hand coordinate system. First, the definitions for the CASI motion stages and coordinate axes are defined in Table 5.

Table 5: CASI motion stages and coordinate axes

Stage	**Definition**
Sample x	Allows the illuminated spot to be positioned at any place on the sample, in conjunction with sample y
Sample y	Allows the illuminated spot to be positioned at any place on the sample, in conjunction with sample x
Sample z	Allows the sample to be centered on the Sample θ/Receiver θ axis
Sample θ	Rotates the sample about the sample y axis
Sample α	Allows the sample to be rotated about the sample normal
Sample tilt (τ)	Allows the sample to be rotated about the sample x axis
Receiver θ Stage	Rotates the receiver through ±180 to take data measurements.
Receiver Aperture Y Stage	Allows the aperture to be centered on the beam in the vertical direction, the positive Y motion direction is defined by vertical upward motion of the focused spot
Instrument Z Axis	Defined by the incident beam, the positive direction is toward the source from the sample or receiver
Focusing Strength	Allows the focused spot to be moved by moving off-axis parabola and spatial filter

All directions of motion are defined by the motion of the illuminated spot on the sample. That is, movement of the sample x stage for which the illuminated spot in the positive x-direction as viewed from the source optics is defined to be positive motion. The stage physically moves in the negative direction. Converting between the CASI coordinates and those defined by Nicodemus requires first describing the incident beam and the receiver location in terms of CASI x-y-z direction vectors. The coordinates are then rotated about the x-axis by $-\tau$ (sample tilt), the y-axis by $-\theta_i$ (sample θ) and the z-axis by α (sample α). The rotated x-y-z values are then converted to spherical coordinates to yield values in the Nicodemus convention. Figure 15 shows the coordinate system from the sample perspective.

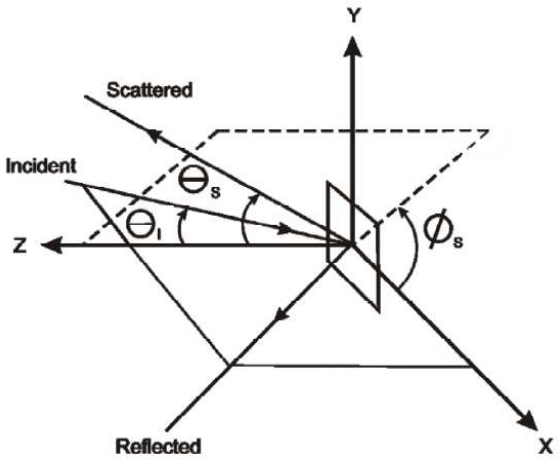

Figure 15: Geometry of scatter (76)

3.6 Calibration of the CASI

A calibration reference file is used to create a baseline for these measurements. This reference scan is taken in air and the results are normalized. The results taken at 633 nm are shown in Table 6 below. This scan gives a baseline for the results in air for the linear polarization (vertical, horizontal, and +/- 45° alignment) as well as circular polarization (right and left-handed). This reference file consists of a matrix of the base-state polarization configurations achievable with the CASI, describing the orientation of the source and receiver polarizations with respect to each other. The linear polarization components are denoted by: V for vertical polarization, H for horizontal polarization, (+) for +45°, and (-) for -45°. The circular polarization components are denoted by R for right-handed circular polarization and L for left-handed circular polarization.

The values are determined via Malus' Law, defined by

$$I = I_0 \cos^2 \theta \qquad [\ 30\ ]$$

where I is the intensity of the transmitted light, I_0 is the intensity of the incoming beam, and θ is the angle between the maximum transmission intensity and the angle of rotation of the polarizer. Generally, I_0 is normalized to 1, therefore

$$I = \cos^2 \theta \qquad [31]$$

The cosine function ranges from -1 to +1, therefore the cosine squared values range from 0 to 1, therefore $-1 \leq \cos\theta \leq +1$ and $0 \leq \cos^2 \theta \leq 1$. From this it follows that an ideal/perfect polarizer would have 100% transmission (I=1). Recall, 100% transmission is expected when the polarization of the incoming light is oriented in the same direction (parallel with) the polarizer it is incident on. Conversely, 0% transmission is expected when they are perpendicular (*I=0*).

For the CASI system, this translates to the case where the source polarization matches the receiver polarization (when they are in parallel), there is full transmission detected. When the source polarization is perpendicular to the receiver polarization, there is almost nothing detected, as seen in Table 6.

Table 6: CASI reference scan of air at 633 nm

		Source Polarization					
		V	H	+	-	R	L
Receiver Polarization	V	1.00	0.01	0.43	0.53	0.47	0.49
	H	0.00	0.99	0.63	0.52	0.60	0.59
	+	0.52	0.43	1.02	0.00	0.55	0.51
	-	0.54	0.64	0.01	1.01	0.52	0.55
	R	0.47	0.60	0.53	0.56	1.05	0.02
	L	0.60	0.45	0.54	0.51	0.00	1.01

As shown in

Table 6, this general format holds true for the vertical and horizontal orientations. However, as they are not perfect/ideal polarizers there is a deviation from the ideal cases as seen in Table 7, where for certain terms in

Table 6, the components are closer to $I = 0.4, 0.6$.

Table 7: Standard Deviation of Air Reference

Malus' Law	**Reference Scan alignment**	**Average**	**Standard Deviation**	**Bounds (High, Low)**	**Range**
$I = 1$	VV, HH, ++, --, RR, LL	1.01	0.02	1.05, 0.99	0.06
$I = 0.5$	V+, V-, VR, VL, H+, H-, HR, HL, +V, +H, +R, +L, -V, -H, -R, -L, RV, RH, R+, R-, LV, LH, L+, L-	0.53	0.06	0.64,0.43	0.21
$I = 0$	VH, HV, +-, -+, RL, LR	0.07	0.01	0.02,0.00	0.02

3.7 Dependence on tilt

Many of the ideal cases in the literature deal with on-axis measurements or instances where the beam is incident at normal incidence. However, it is necessary to account for any off-axis measurements or tilted sample measurements as well since field testing situations and real-world applications are more likely to have non-normal incidence. These non-ideal situations must be accounted for a more thorough understanding of the data, both as a basis for future laboratory experiments, field testing and applications as well as implementation in any future sensor or algorithm optimization. The CASI User Reference Manual (76) defines tilt as the rotation about the sample's x-axis, shown in Figure 16, and therefore any rotation about the y-axis is a

relation to angle of arrival. No tilt (zero) occurs when the laser beam is at normal incidence to the sample.

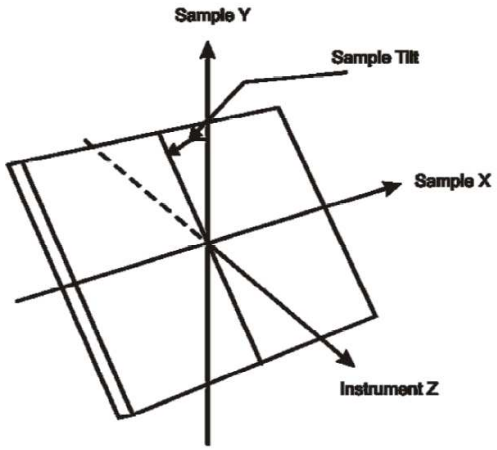

Figure 16: Sample tilt axis

For the determination of any potential tilt effects on the sample measurements, we start with the general form of the Electric field shown in equation below.

$$\vec{E} = E_x\hat{x} + E_y\hat{y} + E_z\hat{z} \qquad [32]$$

The laser is propagating in the z-direction, therefore, the electric field is perpendicular to the direction of propagation, therefore the E-field will only exist in the x & y directions:

$$\vec{E} = E_x\hat{x} + E_y\hat{y} \qquad [33]$$

The laser for the scatter measurements in the CASI system is initially horizontally polarized therefore this equation reduces the electric field even further to:

$$\vec{E} = E_x\hat{x} \qquad [34]$$

The Stokes vector equivalent for horizontal polarization is

$$S = \begin{bmatrix} 1 \\ 1 \\ 0 \\ 0 \end{bmatrix} \qquad [35]$$

The normal to the sample is rotated through angle φ, therefore the angle of incidence becomes θ + φ. The difference between the angles of incidence (normal and tilted) is 2φ. For rotation about the x-axis, the normal to the sample is rotated through angle φ, therefore the total angle of incidence becomes $\theta' = \theta + \varphi$, and the difference between the angles of incidence (original and tilted) is 2φ. Therefore, we can correlate the tilt to that of a rotated linear polarizer with the angle of tilt θ' corresponds to the angle of rotation of the linear polarizer θ. For normal incidence, this implies Malus' Law becomes a function of θ':

$$I = I_0 \cos^2(\theta') \qquad [36]$$

While the E-field is still solely in the x-plane, there is a portion of it projected onto the y - plane due to the sample tilt. This component will be a function of the tilt

$$E_y = \tan(\theta') / E_x \qquad [37]$$

Based on the tangent values from Equation 37 above, we see small residual tilt does not have a large impact, as seen in Figure 17.

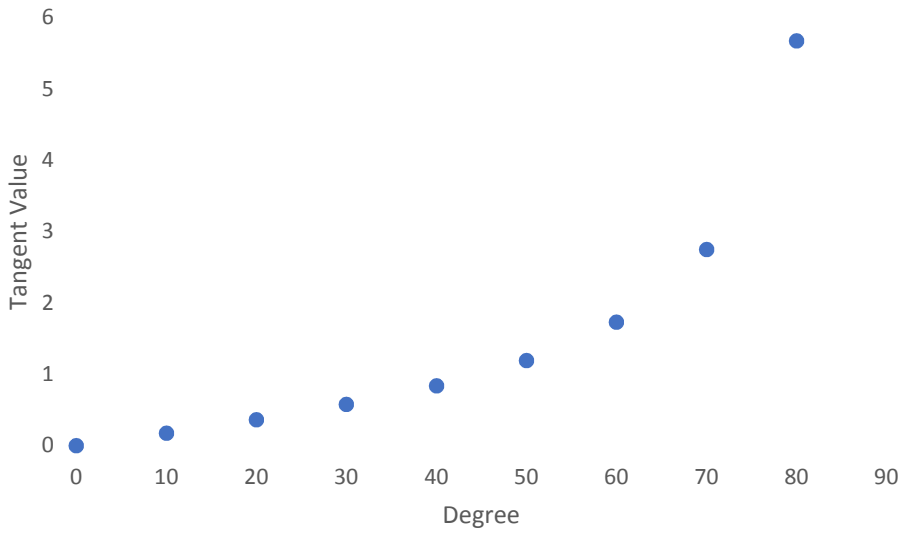

Figure 17: Total angle of incidence as a function of angle of incidence and tilt

3.8 CASI data

3.8.1 Silicon wafer

For error analysis, data was first taken for a silicon wafer as it is an isotropic sample (uniform in all directions). The matrix for an ideal isotropic sample is a diagonal matrix, with all non-diagonal elements equal to zero. It is compared to the data taken from an J. A. Woollam WVASE32 ellipsometer. This machine operates similarly to the CASI in that it uses light as a non-contact probe to and measures the change in polarization of a beam upon reflection or transmission from a sample. Most ellipsometry follows the Verdet convention, which utilizes a right-handed basis such that the Fresnel reflection coefficients are defined as $r_\perp = r_s = -r_p$ opposed to the lesser used Fresnel convention where $r_\perp = r_p = r_s$ (78).

The general Mueller Matrix for isotropic media in ellipsometry (79) is given by

$$M_{sample} = \begin{bmatrix} 1 & -N & 0 & 0 \\ -N & 1 & 0 & 0 \\ 0 & 0 & C & S \\ 0 & 0 & S & C \end{bmatrix} \quad [38]$$

where

$$N = \cos(2\psi) \quad [39]$$

$$S = \sin(2\psi)\sin(\Delta) \quad [40]$$

$$C = \sin(2\psi)\cos(\Delta) \quad [41]$$

$$1 = N^2 + S^2 + C^2 \quad [42]$$

The measured data is then compared to theoretical calculated model of the sample to determine parameter such as film thickness, roughness, etc. Figure 18 below shows these ellipsometry results for the Si wafer at 632.8 nm. We see that linear diattenuation a (m_{01}, m_{10}) elements have angle dependence, while all other off-diagonal elements are zero. Note, the ellipsometer does not measure components c m_{30}, e m_{31}, and f m_{32} but has theoretical-model-calculated values for those components, approximately equal to zero.

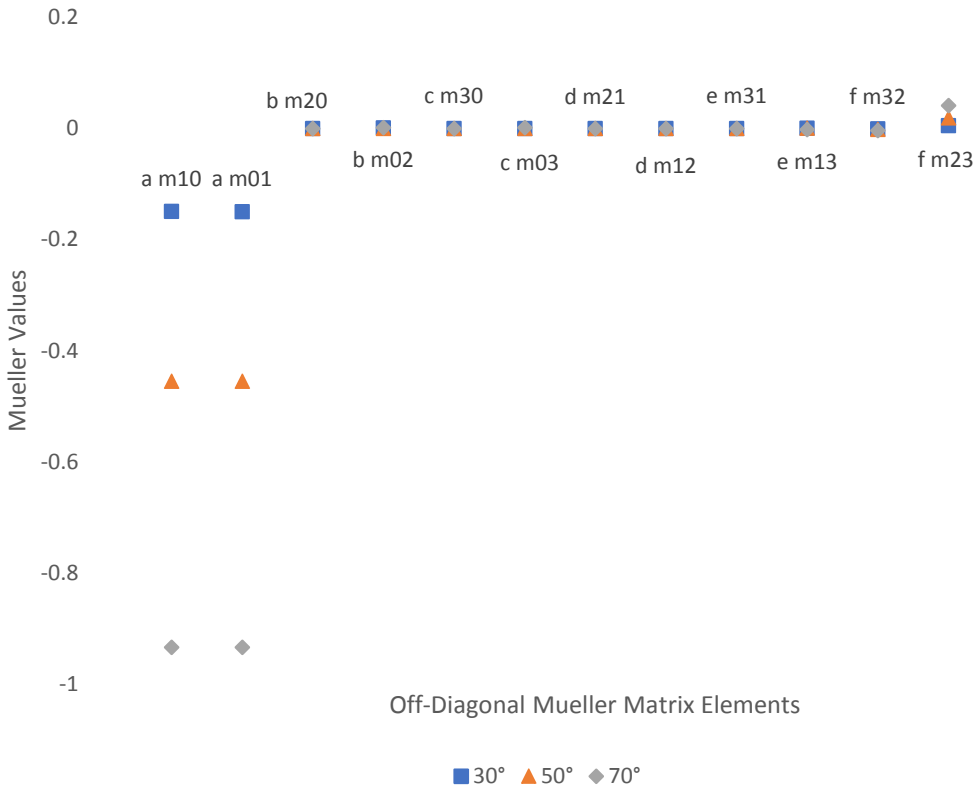

Figure 18: Ellipsometry Measured Mueller Matrix of an Si Wafer

Below, Figure 19 shows the results from Laskarakis et. al (80) where they detailed Mueller element dependence on incident energy (wavelength) from 1.5–6.5 eV (826.7 nm to 190.8 nm) for an Si wafer via Mueller matrix ellipsometry at 70°. Laskarakis et. al states the results of the Si Mueller matrix are "nearly ideal" with near-zero off-diagonal elements and $m_{12} = m_{21}$, $m_{33} = m_{44}$ and $m_{34} = -m_{43}$. They account for the "slight" discrepancies in the polarization from an ideal isotropic sample in the low-energy range as possibly a result of calibration artifacts in that portion of the spectrum. The value relevant to our ellipsometry measurements (632.8 nm) and CASI measurements (633 nm) is 2.0 eV, and therefore fall in that range and will be subject to the same calibration artifacts. The Laskarakis et. al. results at 2.0 eV and 70° are concurrent with the results measured on the WVASE32 ellipsometer at 70°, with the a (m_{01}, m_{10}) elements

approximately equal to negative one and the remainder of the off-diagonal results equal to zero.

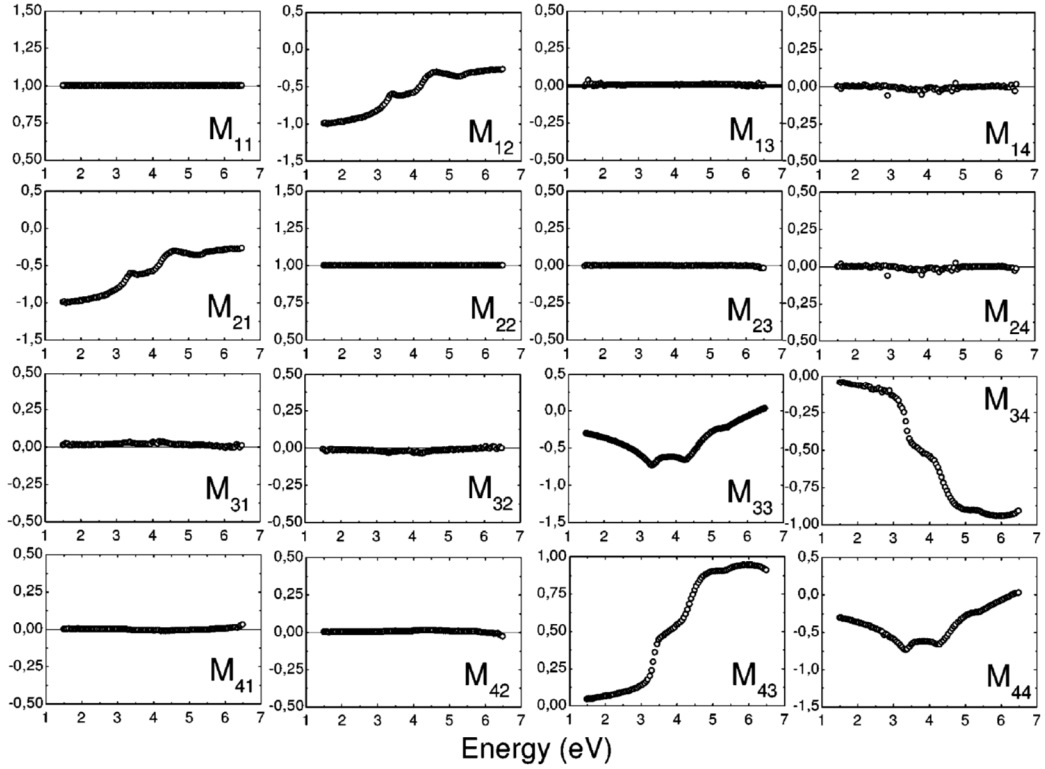

Figure 19: Si wafer at 70° Laskarakis 2004 (76)

The results from the CASI are shown in Figure 20 below. At 70°, the a (m_{01}, m_{10}) elements approximately equal to one. The *a* (m_{01}, m_{10}) values of the CASI fall within the standard deviation calculated for the CASI in

Table 6 (±0.06). The amplitude/absolute values for linear diattenuation *a* (m_{01}, m_{10}) from the CASI values and both the ellipsometry values are approximately one, which also indicates the CASI is appropriately calibrated for the linear diattenuation values. The remainder of the off-diagonal results approximately equal to zero with the linear diattenuation in *b* (m_{20}) and linear retardance in *d* (m_{21}, m_{12}). The error *b* (m_{20}) is most

likely an artifact of both the calibration in this portion of the spectrum as well as the imperfections in the polarizers, seen in the CASI reference files and calibration in

Table 6 and Table 7. These tables also show imperfections in the polarizers are more evident in the cross components such as would be the case for the linear retardance in *d* (m_{21}, m_{12})

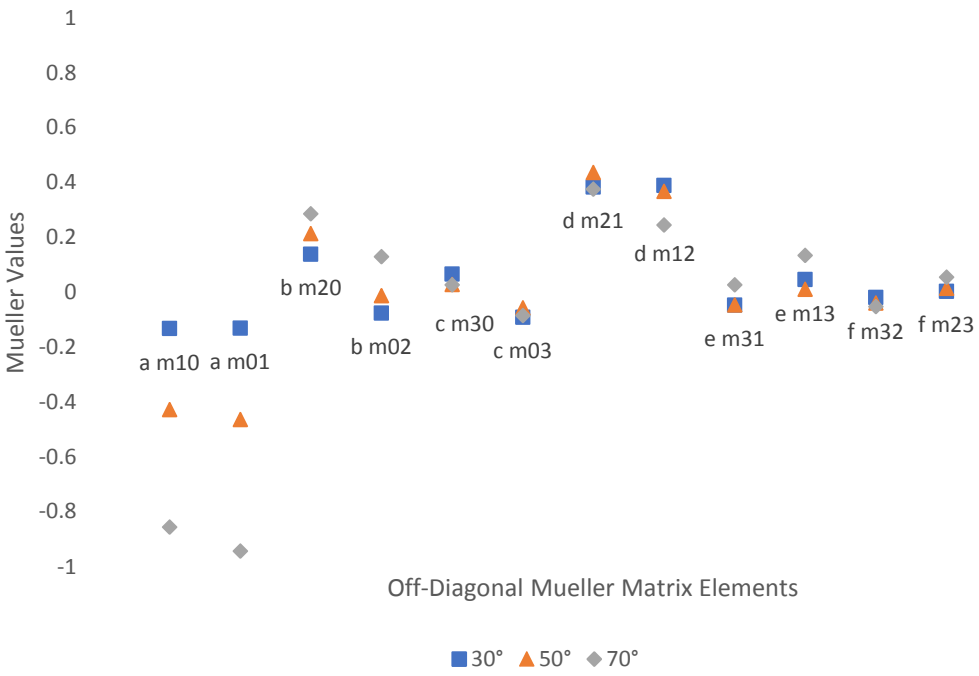

Figure 20: CASI Measured Mueller Matrix of an Si Wafer

For a closer look at the data, we examine Figure 21 through Figure 23. We see that the imperfections in the polarizers cause consistent presence of linear retardance *d* (m_{21}, m_{12}), mostly independent of angle whereas the angle of incidence plays a large role in the linear diattenuation components.

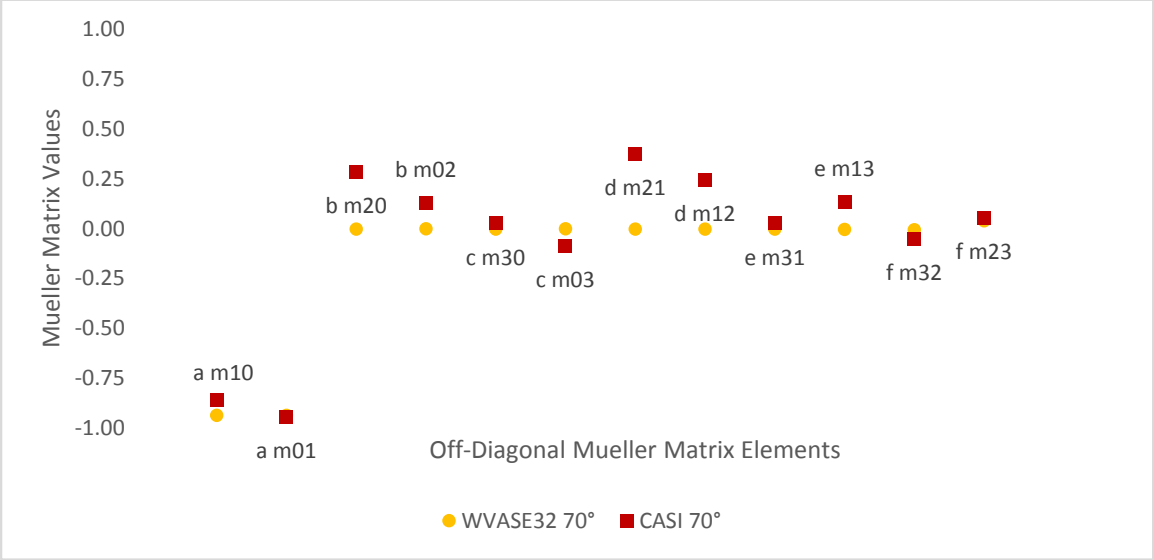

Figure 21: 70° comparison of VASE, CASI

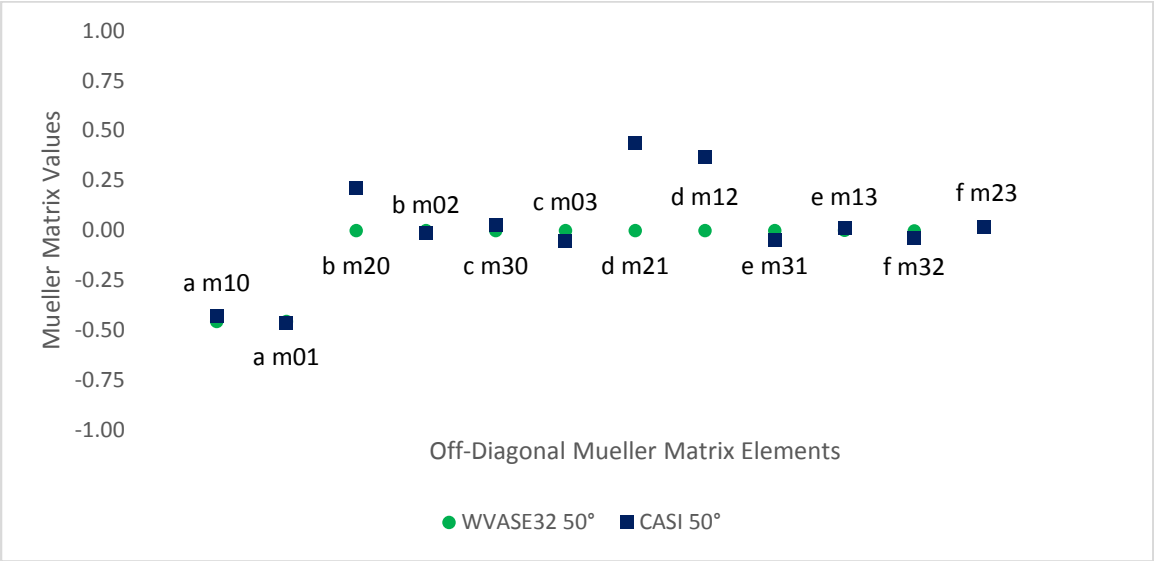

Figure 22: 50° comparison of VASE & CASI

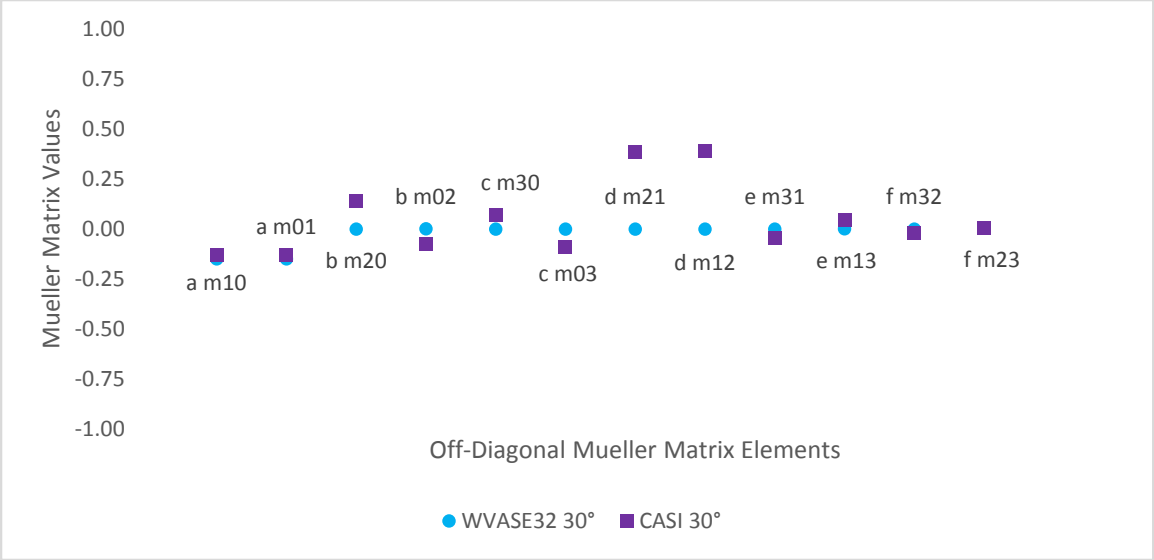

Figure 23: 30° comparison of VASE & CASI

3.8.2 Dove Prism

A Dove prism is a reflective prism used to rotate and invert an image or retroreflect light. An unmounted dove prism (part number: PS992-A from Thorlabs) was tested, shown in Figure 24. It is a 15 mm square cross section made from N-BK7 glass.

Figure 24: Dove Prism

Moreno 2003 (64) analyzed changes to linearly polarized light passing through a Dove prism from a Jones calculus perspective. As shown in Figure 25, light is incident on one leg of the prism and exits the opposite side.

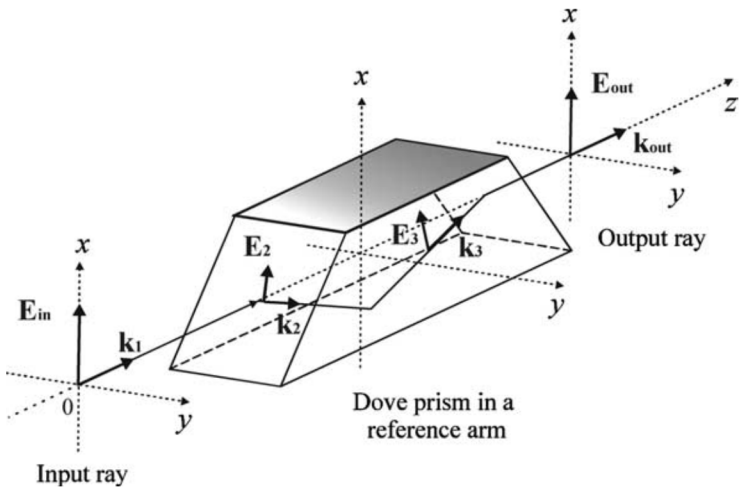

Figure 25: Linear polarization along the x-direction maintains its state of polarization after transmission through a Dove prism (64)

Moreno et. al. rotated the Dove prism about the z axis, as shown in Figure 26 below, where φ denotes the angle of rotation. This is also the configuration used for the CASI experiments.

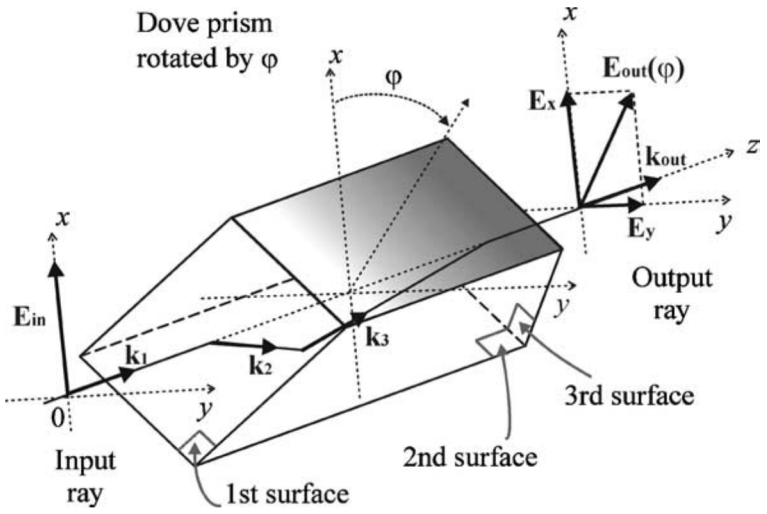

Figure 26: Dove prism rotation about z-axis (64)

According to their findings, Figure 27, linearly polarized light changes into "mildly" elliptically polarized light (64). As mentioned above in Section 3.1, a QWP is an optical

element that converts linearly polarized light to elliptically polarized light, and vice versa. The findings in Moreno et. al. (64) suggest the dove prism acts as an imperfect QWP, which would make the Dove prism a retarder. Therefore, we expect to see changes in the "*f*" components of the Dove prism's Mueller Matrix. Note, the convention detailed in Moreno et. al. Figure 27 is for twice the angle of rotation φ (recall φ is defined as the angle of rotation about the z-axis in Figure 26). Table 8 below shows the corresponding angles for the CASI data and Moreno et. al.

When the prism is positioned at 0° or 90° of rotation the input polarization is equal to the output polarization. These angles correspond to the Dove prism oriented as shown in Figure 25, and Figure 26, respectively. The angles at which the most significant polarization change occurs is at 45° and 135°, where the polarization is elliptical and the closest to circular it can be.

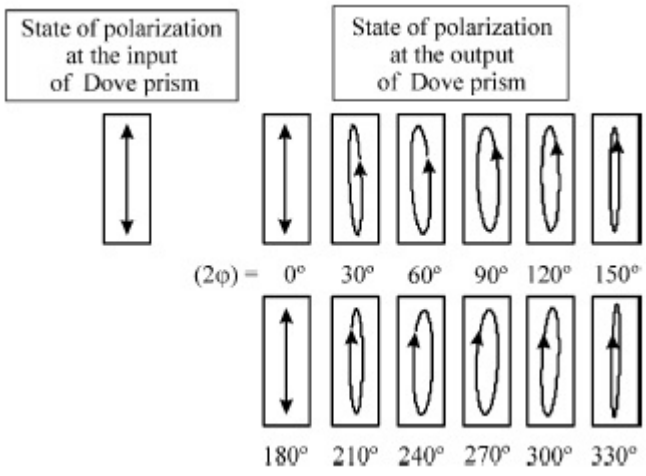

Figure 27: Polarization conversion of a Dove Prism (64)

Table 8: Angles of Rotation for the Dove Prism

CASI Angle (Figure 28)	**Moreno** et.al. (Figure 27)
0°	0°
30°	60°
45°	90°
60°	120°
90°	180°

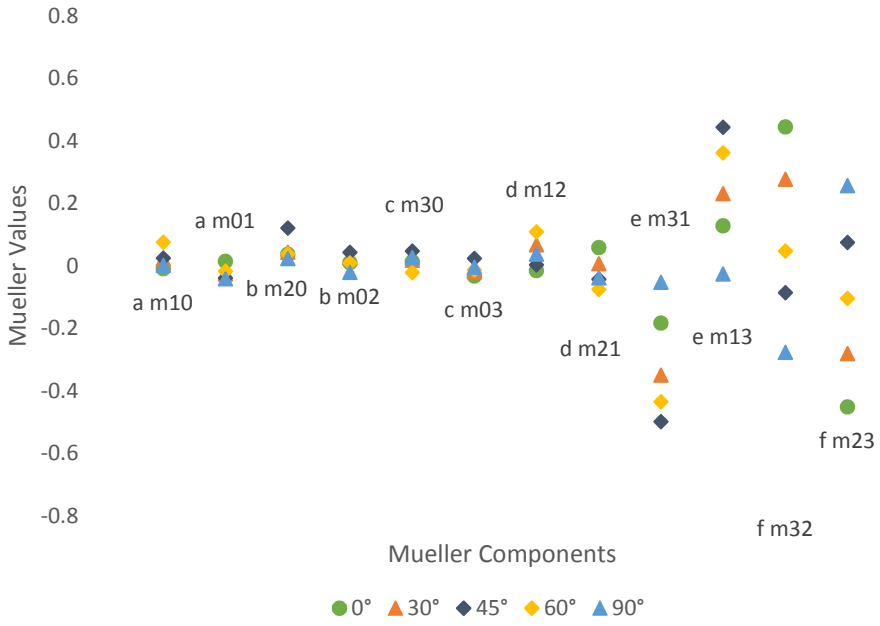

Figure 28: Off-diagonal Mueller Matrix components of a Dove Prism

The Mueller components related to retardation are *d*, *e*, and *f*. As seen in the CASI data results in Figure 28, there is a similar angle of rotation dependence for linear and circular retardance, confirming the Dove prism acts as a retarder. A closer look at these elements is shown in Figure 29. The "slightly elliptical" polarization discussed in Moreno et. al (64) is evident here, as the circular retardance values *f* (m_{32}, m_{23}) range from

approximately -0.6 to +0.6, whereas fully elliptical polarization would have values close to ±1. The peak polarization changes shown in Moreno et al. (64) occurs at $\varphi = 90°$ ($\theta = 45°$ in our nomenclature) for vertically polarized light. Therefore, the opposite would be true, with peak polarization change at $\theta = 45°$ for horizontally polarized light, which is shown in the CASI measurements.

The linear retardance $e\ (m_{13}, m_{31})$ that occurs as the light transverses the prism is not an artifact accounted for in Moreno et al. (64), however, Yun et al. (65). handles the retardance of a Dove prism via 3D raytracing and Jones matrices based on angle of rotation (65). Based on the equation for a rotated retarder, shown in Section 3.1, we see that $f\ (m_{32}, m_{23}) \approx \mp sin\,\varphi\, cos\,2\theta$ and $e\ (m_{13}, m_{31}) \approx \pm sin\,\varphi\, sin\,2\theta$. From this we see the cosine/sine dependence implies as one rises the other falls, which we see in Figure 29.

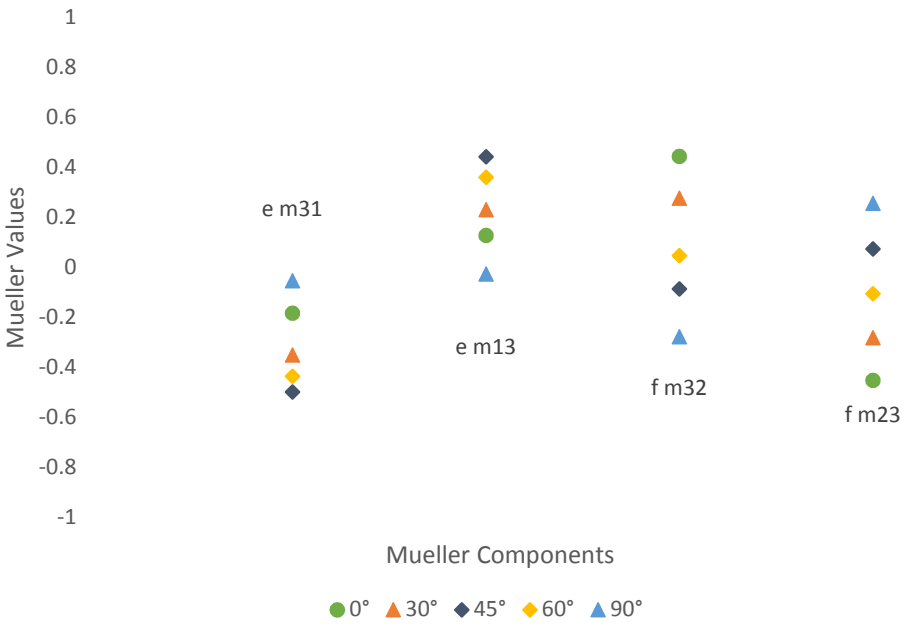

Figure 29: Linear and circular retardance in a Dove Prism

3.8.3 Cornercube Reflector (CCR)

The CCR consists of three perpendicular reflective (mirror) surfaces which, due to the geometry causes incident light to be reflected directly back in the direction of the source, as shown in Figure 30.

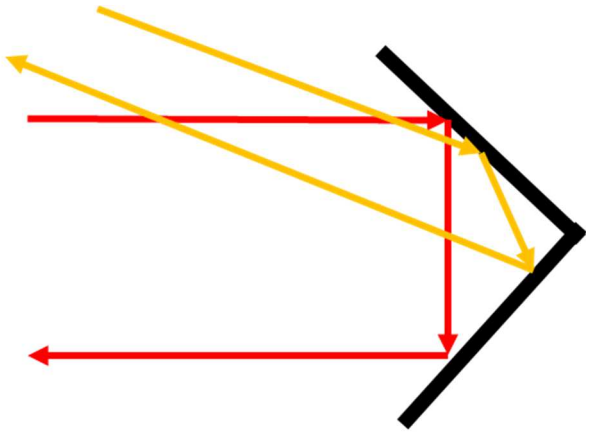

Figure 30: CCR ray trace diagram

Kalibjian et al. (62) discuss how a CCR can cause various polarization changes. The CCR is another optical element that changes polarization from linear to elliptical & elliptical to linear similarly to a QWP/retarder. Kalibjian et al. explains even slight changes in the CCR orientation (including rotation, beam angle, or beam off-set) can potentially have significant changes on the polarization. From Kalibjian et al., the general form of the Mueller matrix for an ideal metal-coated CCR is shown below, where φ is the phase change.

$$M_{\substack{ideal \\ metal-coated \\ CCR}} = \begin{bmatrix} 1 & 0 & 0 & 0 \\ 0 & -\cos\varphi & -\sin\varphi & 0 \\ 0 & -\sin\varphi & \cos\varphi & 0 \\ 0 & 0 & 0 & -1 \end{bmatrix} \qquad [\,43\,]$$

This matrix is similar to that for a rotator, with the center block consists of cosine and sine terms. The difference is here there are additional negative signs for m_{11} and m_{12}, whereas the Mueller matrix for a rotator only has a negative sign for m_{21}.

From Kalibjian et al., the phase change is approximately 60°, which yields

$$M_{\substack{metal-coated\ CCR, \\ on-axis}} = \begin{bmatrix} 1 & 0 & 0 & 0 \\ 0 & 1 & 0 & 0 \\ 0 & 0 & -1 & 0 \\ 0 & 0 & 0 & -1 \end{bmatrix} \quad [\ 44\ ]$$

for on-axis measurements.

For the CASI Mueller matrix measurements, we use a gold coated, aluminum replicated hollow metal retroreflector from Newport Optics (part number: 50394-2530) shown in Figure 31.

Figure 31: Au coated CCR

These results are shown in Figure 32 below. When the angle of incidence is zero, the values are near-zero. These results agree with Kalibjian et al.'s findings where the off-diagonal values for on-axis measurements are zero. The higher values for linear retardance reflect the previously discussed aggregate errors from the multiple polarizers

in the CASI as well as the non-ideal nature of the CCR. As the angle of incidence increases, retardance elements arise similar to what is seen for rotated retarders.

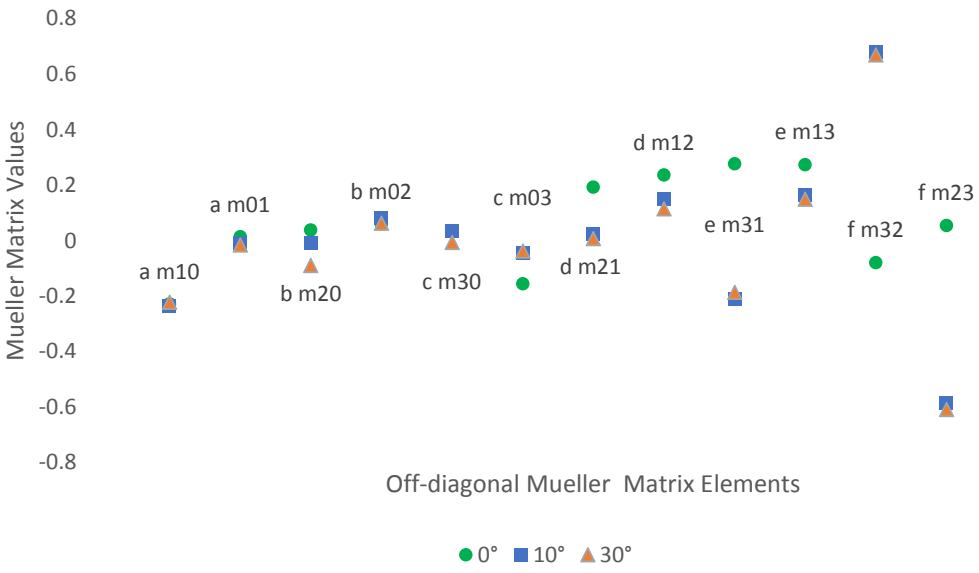

Figure 32: Off-diagonal Mueller Matrix Components of an Au-Coated CCR

3.8.4 Retroreflective Tape

O'Brien et al. (81) examined polarization properties of retroreflective materials, via several polarization maps, which show intensity and polarization rotation are functions of angle of incidence for various polarization states. Specifically, both intensity and rotation decrease as the angle of incidence increases, as shown in Figure 33 and Figure 34 below. The contours show the intensity of the returned beam relative to its maximum in decibels. O'Brien et al. also notes that whichever polarization state is incident on the material, there will be some component of the opposite state present upon reflection due to the geometric nature of the material (retroflecting sheets are structured to mimic an array of retroreflecting items such as, glass beads, microprisms, CCRs, etc). For example, if horizontal polarization is incident, there will be both horizontal and

vertical reflected back. However, the change in the intensity of the opposite polarization with respect to angle of incidence is much smaller than that of the state of the original polarization orientation, i.e. when horizontal polarization is incident, the vertical component returned is much smaller than the horizontal component returned. O'Brien et al. decompose the angle of incidence into azimuth angle and elevation angles, which here we simply call angle of incidence and tilt, respectively. Note there is no polarization rotation for an ideal reflective structure due to the fixed π phase change on reflection at any interface independent of incidence angle, therefore some degree of polarization rotation is expected for all non-ideal components (81). For the purposes of this dissertation, we will focus on the positive azimuth angles only (the elevation angle is equal to zero, since we did not acquire data as a function of tilt angle).

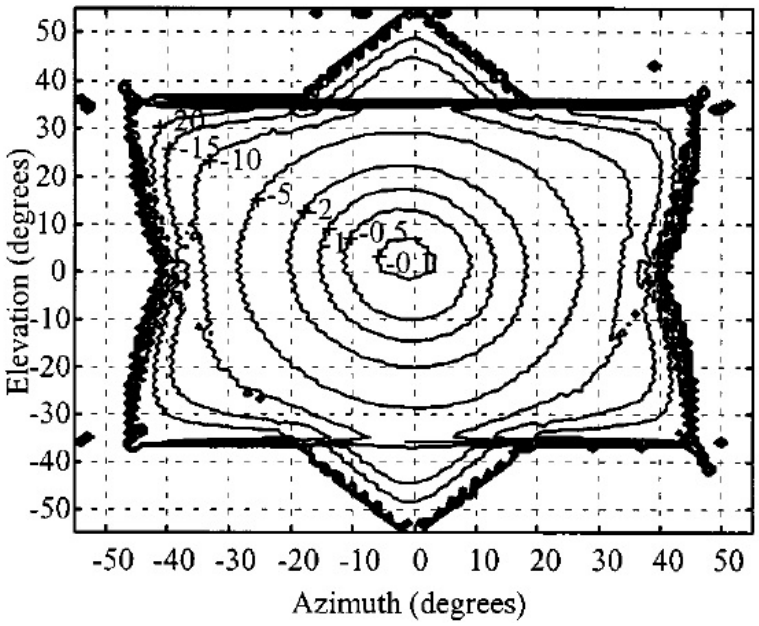

Figure 33: Measured intensity of returned horizontal polarization versus angle of incidence for retroreflecting sheet illuminated with horizontally polarized light. Contours are in decibels relative to maximum intensity (81).

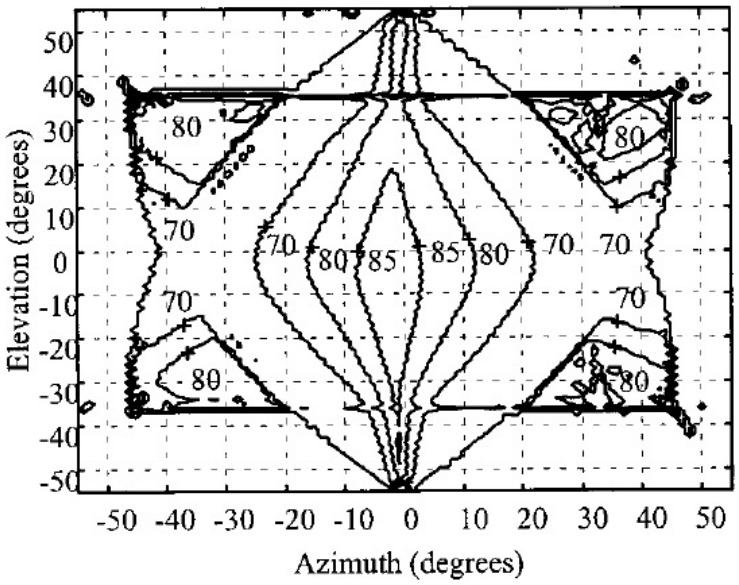

Figure 34: Returned polarization ellipse angle versus angle of incidence for retroreflecting sheet illuminated with horizontally polarized light. Contours are in degrees of rotation relative to vertical direction (81).

For the CASI Mueller matrix measurements, reflective tape is used. The reflective tape is a yellow dot (part number: 6042T29 from McMaster-Carr) 2.5 inches in diameter with 0.025 inches thickness. The CASI results are shown in Figure 35 below. We see the presence of both linear diattenuation *a* (m_{01}, m_{10}) and *b* (m_{02}, m_{20}), as well as linear retardance *d* (m_{12}, m_{21}). Recall, diattenuation is defined as the intensity of the exiting light relative to the input polarization and retardance as the phase change based on polarization (74). From these definitions we see the dependence of linear diattenuation on angle of incidence concurs with O'Brien et al.'s finding of changes in the polarization in both horizontal and vertical directions. The linear retardance dependence on angle of incidence also concurs with O'Brien et al.'s findings of rotation change present upon reflection. As found in O'Brien et al., intensity of the light is more affected by the angle of incidence than the rotation is as well as the appearance of polarization in both the horizontal and

vertical directions. Note, the symmetry in d (m_{12}, m_{21}) implies depolarization is occurring as well.

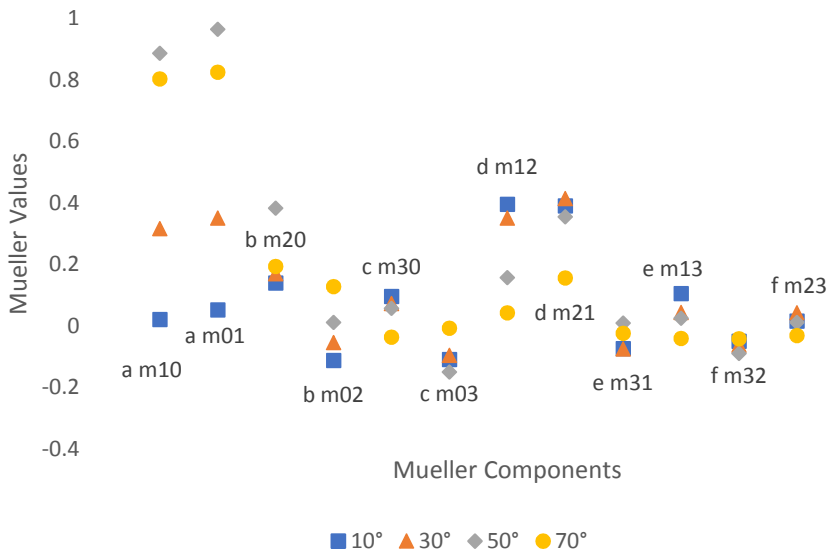

Figure 35: Off-diagonal Mueller Matrix components of Yellow Reflective Tape

3.8.5 Liquid Crystal Beam Steerer

In this dissertation, the Mueller matrix of light reflected a Liquid Crystal Polarization Grating (LCPG) beam steerer retarder switch in operation is analyzed. The LCPG retarder switch is an electrically controlled birefringence (ECB) type of nematic liquid crystal device which can be driven with square wave voltage waveform via a function generator. Figure 36 below shows a diagram and photo of the LCPG (82).

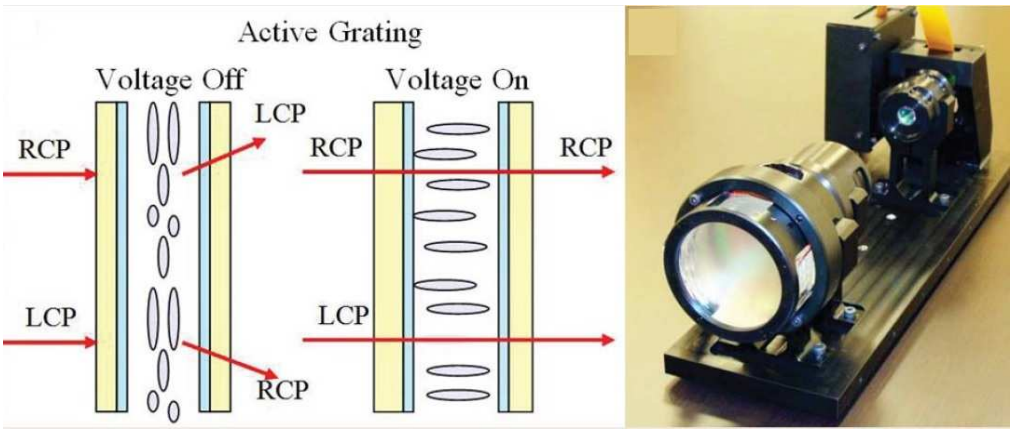

Figure 36: Diagram of LCPG (left); Photo of LCPG (right) (82)

The retardance as a function of voltage is shown in Figure 37 (83). These voltages and corresponding retardation values are used to achieve beam steering when this component is used in conjunction with a diffraction grating (82).

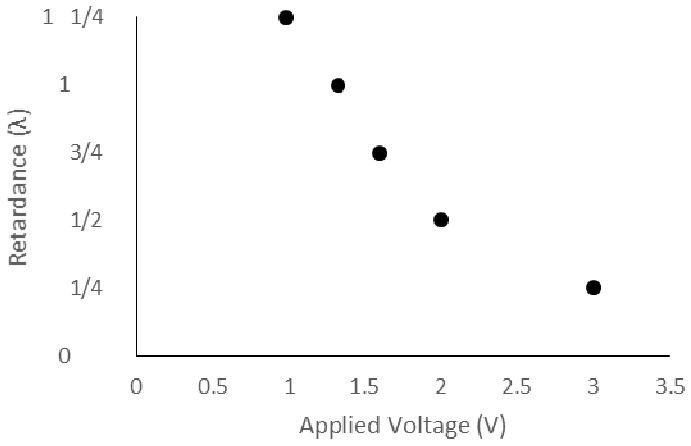

Figure 37: Switch retardance as a function of applied voltage (83)

Harris 2004 (68) and Anisimov 2009 (69) explored polarization effects in a nematic liquid crystal optical phased array (LCOPA) in terms of the Stokes vector.

Harris et al. (68) polarization effects due to director three dimensionality, and oblique angle of incidence operation. Both Harris et al. (68) and Anisimov et al. (69) observed the changes in polarization from the reflected beam due to applied voltage trended from linear to slightly elliptical, which implies retardance present in the LCOPA. Anisimov et al. (69) determined the sensitivity of the beam steering efficiency to tilt angles with respect to the incident beam.

Figure 38 through Figure 42 below detail the off-diagonal Mueller matrix elements of the LCPG beam steerer retarder switch in reflection with various applied voltages and incidence angles, as the reflected signal is what would be detected in a scanning scenario. The analysis of the reflected signal from a Mueller matrix of an LCPG beam steerer retarder switch has not been performed in the literature to date.

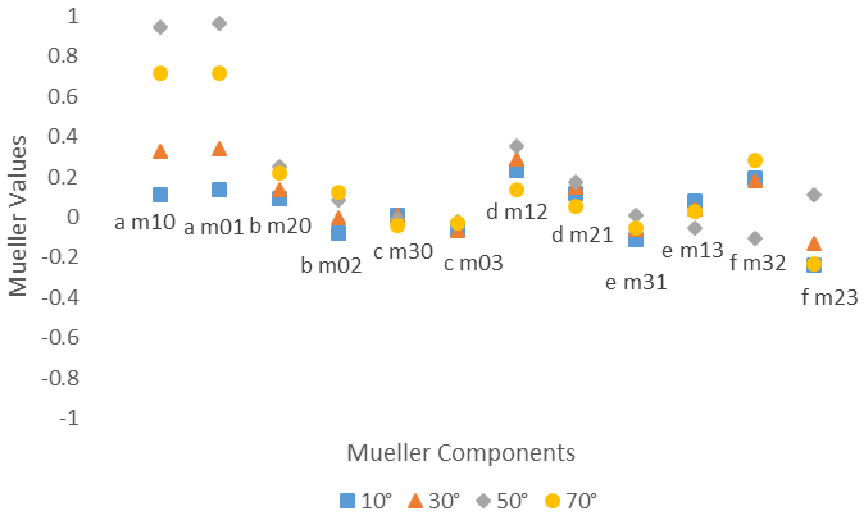

Figure 38: Off-diagonal Mueller Matrix Components of an LC retarder switch in reflection with no voltage applied

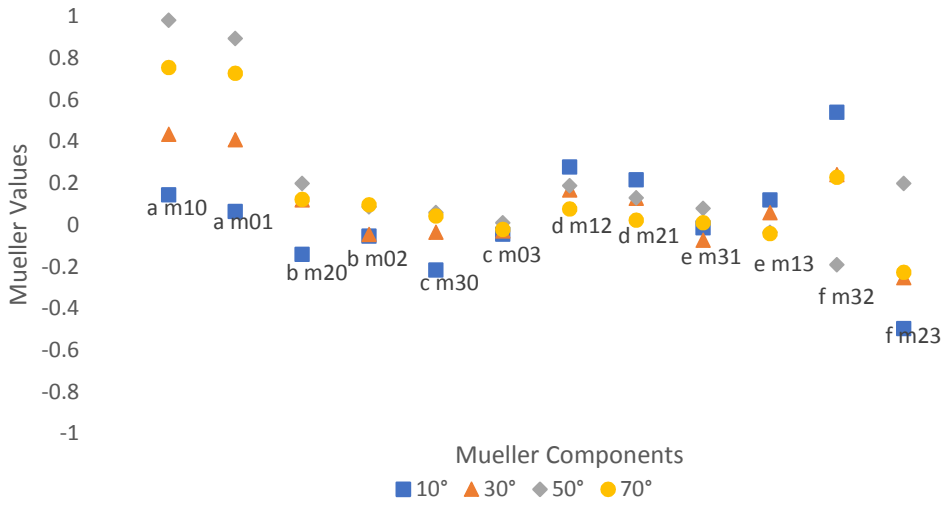

Figure 39: Off-diagonal Mueller Matrix Components of an LC retarder switch in reflection at 1.3V

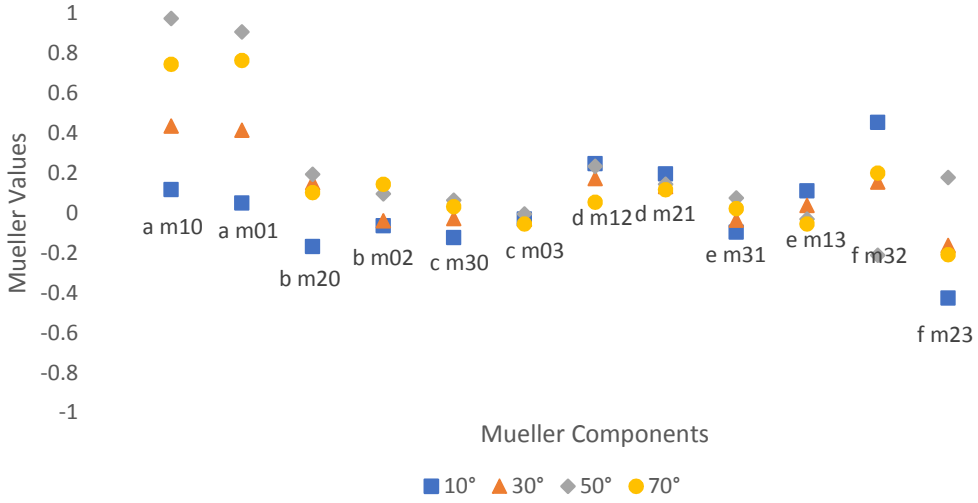

Figure 40: Off-diagonal Mueller Matrix Components of an LC retarder switch in reflection at 1.6V

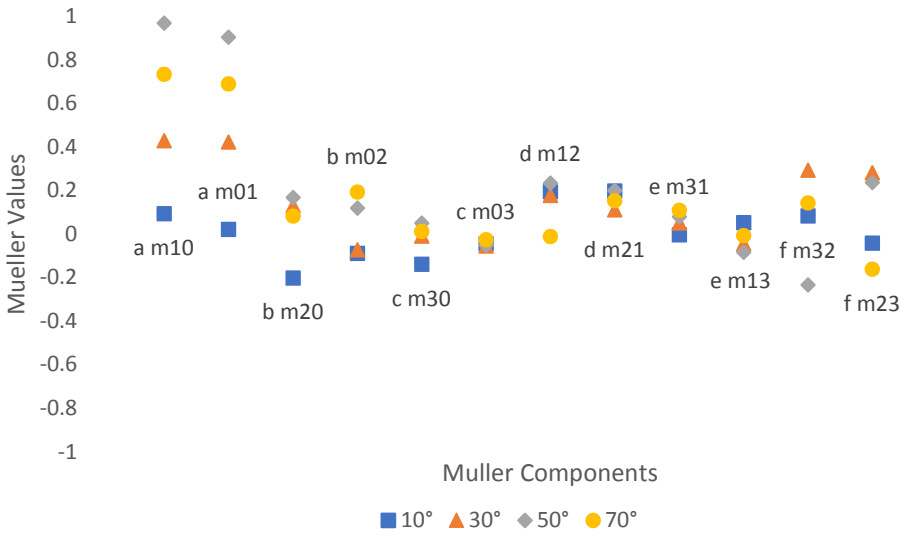

Figure 41: Off-diagonal Mueller Matrix Components of an LC retarder switch in reflection at 2V

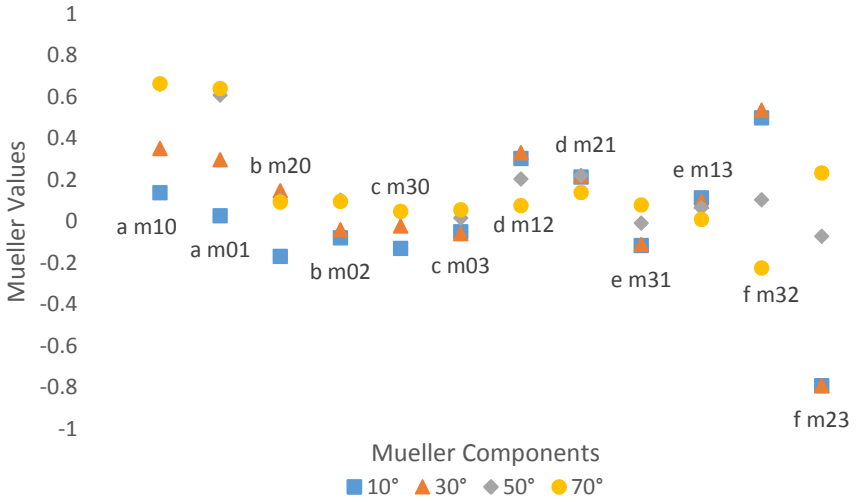

Figure 42: Off-diagonal Mueller Matrix Components of an LC retarder switch in reflection at 3.0V

As shown in the figures above, linear diattenuation and circular retardance are the most affected by angle of incidence and applied voltage, respectively. To take a closer look at these two elements, we compare them to the results for the LCOPA in Anisimov

et al. (69), where they observed changes in polarization from the reflected beam due to applied voltage trended from linear to slightly elliptical, which implies retardance present in the LCOPA.

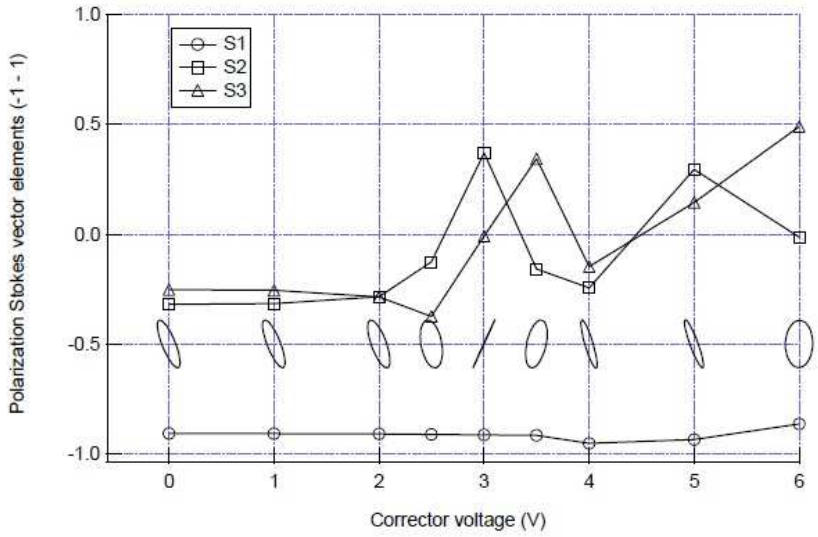

Figure 43: Polarization state of the first diffraction order as a function of the uniform voltage applied to all phase corrector (69)

We see that the S_1 Stokes parameter associated with linear diattenuation does not change significantly with applied voltage, but S_3 Stokes parameter associated with circular retardance does, as shown in Figure 44 and Figure 45 below. The change in circular retardance also concurs with the switch retardance and applied voltage relationship shown previously in Figure 37. We see the most sensitive Mueller matrix elements to angle of incidence were the linear diattenuation a (m_{01}, m_{10}) whereas the circular retardance f (m_{32}, m_{23}) is most sensitive to applied voltage.

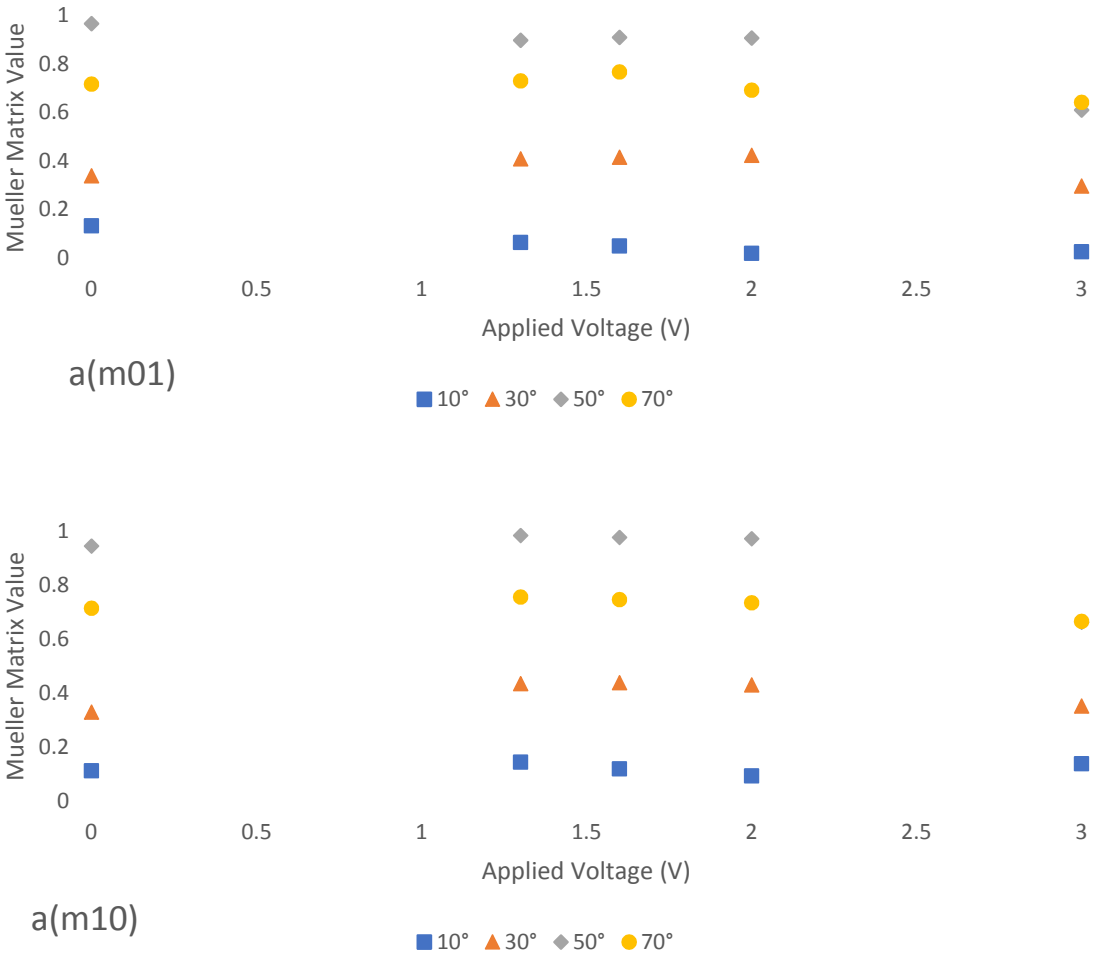

Figure 44: Linear diattenuation Mueller Values of LCPG m_{01} & m_{10}

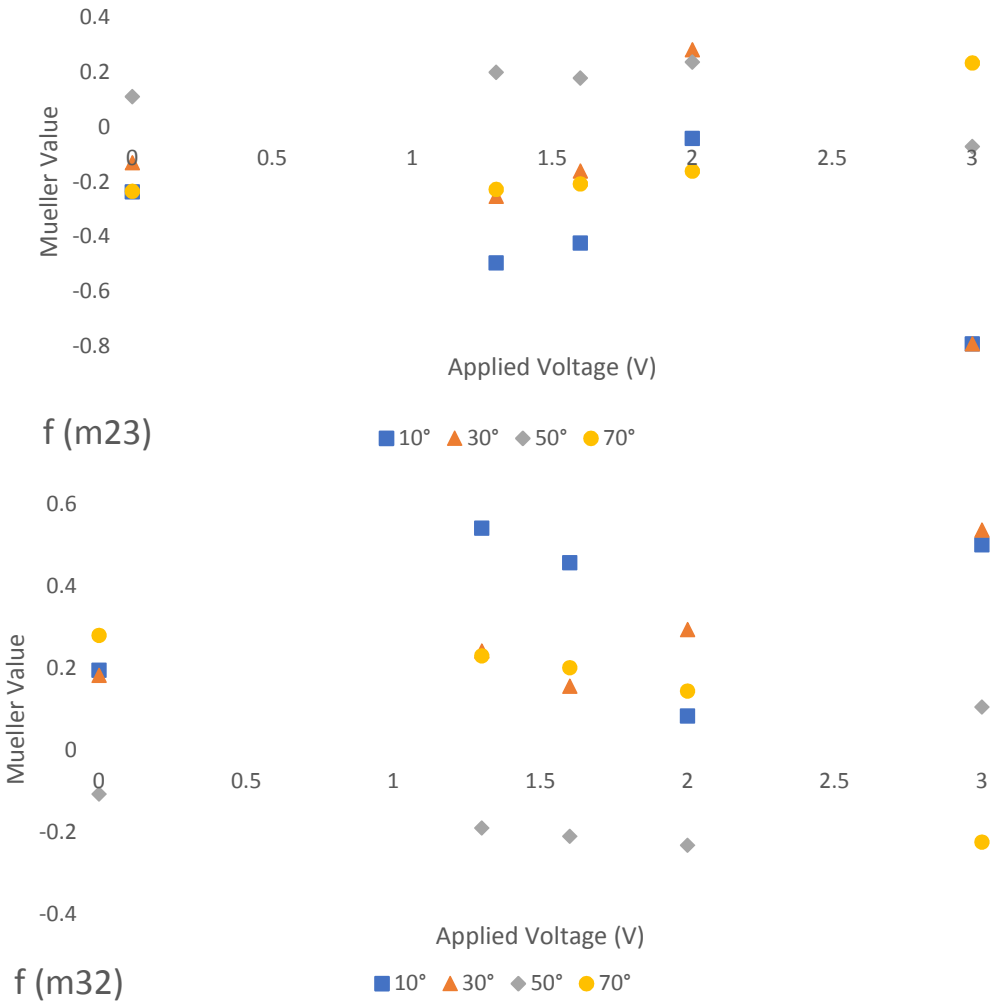

Figure 45: Circular Retardance Mueller Values f (m_{32}) and f (m_{23})

CHAPTER 4: DISCUSSION

Chapter 2 of this dissertation focused on the effects of aliasing on a sensor. When the QCL was modulated at the same frequency as the sensor frame rate, the constructive and destructive interference between the frame rate and modulation frequency of the laser were similar to a beat frequency effect. This lays the groundwork for methods analogous to the frequency-hopping used in transmitting radio waves for furthering solutions for anti-aliasing problems. Performing additional FINC tests at different frame rates will allow for further optimization of the autonomous sensor algorithm development. Next steps would be to test the algorithm with more complex scenarios with a dedicated scene projector, to enhance the discrimination capabilities of the algorithm for static and dynamic scenes and sources as well as for improving clutter rejection. Further testing on the anti-aliasing algorithm will include accounting for heat reflections on metallic surfaces and other heat sources in the frame. The sensor itself may contain characteristics and structures that would cause variation between results in the x and y directions. These test methods can provide the necessary stressing needed to ensure sensors are operating at optimal thresholds. The anti-aliasing techniques discussed above provide the groundwork for future experiments, which will include improvement upon the current algorithm, allowing for discrimination between multiple input signals.

Chapter 3 explored the methodology of the Mueller matrix, analysis of the CASI system and analysis of the Mueller matrices of various samples. Calibration of the CASI determined non-ideal components, contributing to linear retardance in the vertical and horizontal directions. Analysis of a Silicon wafer on both the CASI and an ellipsometer confirm the linear retardance contributed by non-ideal polarizing components in the

CASI. Analysis of the Dove prism on an incoming horizontally polarized beam shows the QWP-like effects it displays as it is rotated about the z-axis. This analysis has expanded the literature beyond the Jones vector analysis contributed by Moreno et. al (64) to include the Mueller analysis. Changes in circular retardance observed in the CCR confirms Kalibjian (62) where the CCR changes polarization from linear to elliptical similarly a QWP/retarder as well as the Dove Prism discussed in Section 3.7.2 above. Both linear retardance and circular retardance angle of incidence dependent. The CCR and the Dove prism Mueller matrix results are distinguishable, though they each have linear and circular retardance affects. The Dove prism can exhibit a larger variety of changes to the polarization at a wider angle range than the CCR, whereas the CCR is more susceptible to tilt.

For the LCPG BS retarder switch, rotation between linear and elliptical polarized light is observed, specifically change in linear diattenuation and circular retardance upon reflection. The analysis of the reflected signal in terms of the LC Mueller matrix of an LCBS retarder is an addition to the literature that will aid in the characterization of signal degradation and polarization back scatter.

The three external characteristics that showed the most influence on the results are angle of incidence, angle of rotation, and applied voltage. Grouping of the relevance of these characteristics are show in

Table 9 below.

Table 9: Grouping of Mueller Component Characteristics

Group #	**Characteristics**
Group 1	Primary characteristics which show significant changes that directly correspond to an external factor
Group 2	Secondary characteristics which show changes are not as evident as Group 1 but could still potentially be used to discriminate beyond Group 1
Group 3	Tertiary characteristics which are present but do not change
Group 4	Quaternary characteristics which show changes in the Mueller component pairs (accounting for symmetry/asymmetry)
Group 5	Quinary characteristics which are unchanging and or zero/near-zero values

Applying these groups to the five samples analyzed in this dissertation, as shown in Table 10, we see each sample has distinguishable characteristics from the other.

Table 10: Grouping of Sample Characteristics

	Si Wafer	**Dove Prism**	**CCR**	**Retroreflective Tape**	**LCPG**
Group 1	*-a*	*e, f*	*F*	*+a*	*+a, f*
Group 2		*d*			*a*
Group 3					*d*
Group 4			*E*	*b, d*	*e*
Group 5	*b-f*	*a-b*	*a-d*	*c, e, f*	*b, c*

The measured characteristics of the various samples presented here may be useful in the optimization of detection/discrimination algorithms within remote sensing scenarios where it is desired to discern source emission characteristics in the presence of background or interference. Suggested paths forward include testing at various simulated distances, such that the central airy disk may be observed. This will alleviate any false positive/negative return signals from the return beam. The follow-on research should continue along the two-pronged approach. Testing of various polarizing materials, polarization sensitive materials and other devices such as bolometer arrays, pyroelectric arrays, and holographic diffusers is recommended, along with an analysis of distribution vs single point is recommended as well. Modeling and simulations to account for turbulence in the atmosphere would also be useful. These suggestions and the results of those follow-on experiments would be used to inform future laboratory field-testing scenarios and applications as well as refining any algorithms used to distinguish the pre-determined characteristics from the groupings determined in this dissertation. The completed techniques (beginning with aliasing/anti-aliasing algorithm) will be transitioned to the current and ongoing efforts. These combined efforts support the current and future research by gaining data and insight into the feasibility of enhanced, autonomous platform optimization.

REFERENCES

1) S. Suchalkin, G. Belenky and M. A. Belkin, "Rapidly Tunable Quantum Cascade Lasers," IEEE Journal of Selected Topics in Quantum Electronics, 21(6), 1-9 (2015).

2) Z. Xiao, Q. Wang, G. Zhou, and J. Yu, "Aliasing detection and reduction in plenoptic imaging," Proceedings of the IEEE Conference on Computer Vision and Pattern Recognition, 3326-3333 (2014).

3) M. S. Alam, J. G. Bognar, R. C. Hardie, and B. J. Yasuda, "Infrared image registration and high-resolution reconstruction using multiple translationally shifted aliased video frames," IEEE Transactions on Instrumentation and Measurement 49(5), 915-923 (2000).

4) M. Rachid, S. Pamarti and B. Daneshrad, "Filtering by Aliasing," IEEE Transactions on Signal Processing, 61(9), 2319-2327 (2013).

5) A. Handa, R. A. Newcombe, A. Angeli, and A. J. Davison, "Real-time camera tracking: When is high frame-rate best?" European Conference on Computer Vision, 222-235 (2012).

6) L. Sjöqvist, L. Allard, M. Henriksson, P. Jonsson, and M. Pettersson, "Target discrimination strategies in optics detection," Technologies for Optical Countermeasures X; and High-Power Lasers 2013: Technology and Systems, Proc. SPIE Vol. 8898, 88980K (2013).

7) H-s. Chen, C. R. Nagaraja Rao, and Z. Sekera, “Investigations of the polarization of light reflected by natural surfaces,” Journal of Physics D: Applied Physics, 1(9), 1191 (1967).

8) G. F. Beardsley, "Mueller Scattering Matrix of Sea Water JOSA, 58(1), 52-57 (1968).

9) E. R. Peck, "Polarization properties of corner reflectors and cavities." JOSA 52(3), 253-257 (1962).

10) R. C. Eckardt, and H. Rabin, “Studies of Optical Augmentation with Picosecond Pulses. Picosecond Pulses for Resolution of Optical Elements by Retroreflection,” Naval Research Lab Washington DC Optical Sciences Divison, No. NRL-MR-2298, (1971).

11) J. N. Bradford, and J. F. Giuliani, “Ultrashort Light Pulses in Optical Augmentation,” Naval Research Lab Washington DC, No. NRL-7495 (1972).

12) W. Liebson,"Method and apparatus for blind optical augmentation," US5485012A (1996).

13) W. E. Miller Jr, J. R. Duke, G. W. Starkey, and R. L. Sitton, "Range gated retroreflective missile guidance system," US4234141A (1980).

14) C. S. Naiman, M. King, and M. Greenbaum, "Covert optical system for probing and inhibiting remote targets," US4836672A (1989).

15) R. O. Wilson, "Apparatus and method for highlighting returns from optically augmented targets," US5449899A (1995).

16) T. J. Gleason, "Technique for eliminating undesirable reflections from optical systems," US5629492A (1997).

17) H. M. Reyes Jr, M. B. Haeri, K. K. Colson, R. A. Cesari, T. G. Brauer, and M. C. Menefee, "Detecting a target using an optical augmentation sensor," US20090237668A1 (2011).

18) K. E Schirmer, "Argon laser surgery of the iris, optimized by contact lenses," Archives of Ophthalmology, 101(7), 1130-1132 (1983).

19) M. C. Ertem, D. A. Burchick, T. Ippolito, and D. M. Cordray “A Test Bed for Short Pulse OA Detection of Optical Directors in Amphibious Operations,” Naval Research Lab Washington DC (1999).

20) G. C. Salzman, J. K. Griffith, and C. T. Gregg, "Rapid identification of microorganisms by circular-intensity differential scattering," Appl. Environ. Microbiol., 44(5), 1081-1085 (1982).

21) G. C. Salzman, and C. T. Gregg, "Current and experimental methods of rapid microbial identification," Bio/Technology 2(3), 243 (1984).

22) G. C. Salzman, W. K. Grace, D. M. McGregor, and C. T. Gregg, "An instrument for virus identification by polarized light scattering: a preliminary report," Rapid Methods and Automation in Microbiology and Immunology, 194-197 (1985).

23) W. P. Van De Merwe, D. R. Huffman, and B. V. Bronk, "Reproducibility and sensitivity of polarized light scattering for identifying bacterial suspensions," Applied Optics 28(23), 5052-5057 (1989).

24) G. C. Salzman, C. T. Gregg, W. K. Grace, and R. D. Hiebert, "Biological particle identification apparatus," US4884886A (1989).

25) W-M. Boerner, “Basic concepts of radar polarimetry and its applications to target discrimination, classification, imaging and identification,” Illinois Univ at Chicago Circle Communications Lab, No. UICC-EMID-CL-82-05-18-02 (1982).

26) S. Chaudhuri, B-Y. Foo, and W-M. Boerner, "A validation analysis of Huynen's target-descriptor interpretations of the Mueller matrix elements in polarimetric radar returns using Kennaugh's physical optics impulse response formulation," IEEE Transactions on Antennas and Propagation, 34(1), 11-20 (1986).

27) W. A. Holm, and R. M. Barnes, "On radar polarization mixed target state decomposition techniques," Proceedings of the 1988 IEEE National Radar Conference, 249-254 (1988).

28) J. Cariou, B. Le Jeune, J. Lotrian, and Y. Guern, "Polarization effects of seawater and underwater targets," Applied Optics, 29(11), 1689-1695 (1990).

29) S. Haugland, E. Bahar, and A. H. Carrieri, "Identification of contaminant coatings over rough surfaces using polarized infrared scattering," Applied Optics 31, 3847-3852 (1992).

30) J. Lee,, M. R. Grunes, and R. Kwok, "Classification of multi-look polarimetric SAR imagery based on complex Wishart distribution," International Journal of Remote Sensing, 15(11), 2299-2311 (1994).

31) D Bhanti., S. Manickavasagam, and M. P. Mengüç, "Identification of non-homogeneous spherical particles from their scattering matrix elements," Journal of Quantitative Spectroscopy and Radiative Transfer, 56(4), 591-608 (1996).

32) F. Le Roy-Brehonnet, and B. Le Jeune, "Utilization of Mueller matrix formalism to obtain optical targets depolarization and polarization properties," Progress in Quantum Electronics, 21(2), 109-151 (1997).

33) M. Floc'h, G. Le Brun, J. Cariou, and J. Lotrian, "Experimental characterization of immersed targets by polar decomposition of the Mueller matrices," The European Physical Journal Applied Physics, 3(3) 349-358, (1998).

34) E. Pottier, and J. Saillard, "On radar polarization target decomposition theorems with application to target classification, by using neural network method," Seventh International Conference on Antennas and Propagation, ICAP 91 (IEE), 265-268 (1991).

35) A. H Carrieri., J. R. Bottiger, D. J. Owens, and E. S. Roese, "Differential absorption Mueller matrix spectroscopy and the infrared detection of crystalline organics," Applied Optics, 37(27), 6550-6557 (1998).

36) J. Chung, W. Jung, M.J. Hammer-Wilson, P. Wilder-Smith, and Z. Chen, "Use of polar decomposition for the diagnosis of oral precancer," Applied Optics, 46(15), 3038-3045 (2007).

37) E. Bahar, "Relationships between optical rotation and circular dichroism and elements of the Mueller matrix for natural and artificial chiral materials," JOSA B, 25(2), 218-222 (2008).

38) A. H. Carrieri, J. Copper, D. J. Owens, E. S. Roese, J.R. Bottiger, R. D. Everly, and K. C. Hung, "Infrared differential-absorption Mueller matrix spectroscopy and neural network-based data fusion for biological aerosol standoff detection," Applied Optics, 49(3), 382-393 (2010).

39) F. Cremer, W. de Jong, and K. Schutte, "Infrared polarization measurements of surface and buried antipersonnel landmines," Detection and Remediation Technologies for Mines and Mine-like Targets VI, Proc. SPIE Vol. 4394, 164-176 (2001).

40) B. Ben-Dor, U. P. Oppenheim, and L. Salem Balfour, "Polarization properties of targets and backgrounds in the infrared,"8th Meeting on Optical Engineering in Israel: Optical Engineering and Remote Sensing, Proc. SPIE Vol. 1971, 68-78 (1993).

41) G. Gerhart, and R. Matchko, “Target/background polarization profiles using a COTS digital camera,” Army Tank-Automotive Command Warren MI, No. TACOM-16232 (2000).

42) G. Bieszczad, S. Gogler, and M. Krupiński, "Polarization state imaging in long-wave infrared for object detection," Electro-Optical Remote Sensing, Photonic Technologies, and Applications VII; and Military Applications in Hyperspectral Imaging and High Spatial Resolution Sensing, 8897, 88970R (2013).

43) M. Felton, K.P. Gurton, D. Ligon, and A. Raglin. “Discrimination of Objects Within Polarimetric Using Principal Component and Cluster Analysis,” Army Research Lab, Adelphi, MD, Computational and Information Sciences Directorate, No. ARL-TR-4216 (2007).

44) L. Sadler, and T. A. Alexander, "Mobile optical detection system for counter-surveillance," Ground/Air Multi-Sensor Interoperability, Integration, and Networking for Persistent ISR, 7694, Proc. SPIE Vol. 76940Y (2010).

45) K. Das, A. L. Roy, R. Keller, and G. Tuccari, "Conversion from linear to circular polarization in FPGA," Astronomy & Astrophysics 509, A23 (2010).

46) C. Chun, D. L. Fleming, W. A. Harvey, and E. J. Torok, "Polarization-sensitive infrared sensor for target discrimination," Polarization: Measurement, Analysis, and Remote Sensing, Proc. SPIE Vol. 3121, 55-63 (1997).

47) R. Chipman, “Polarization Diversity Active Imaging,” Proc. SPIE 3170, 68-73 (1997).

48) J. L. Pezzaniti, and R. A. Chipman, "Mueller matrix imaging polarimetry," Optical Engineering 34(6), 1558-1569 (1995).

49) J. L. Pezzaniti, and R. A. Chipman, "Angular dependence of polarizing beam-splitter cubes," Applied Optics, 33(10), 1916-1929 (1994).

50) J. L. Pezzaniti, J. Larry, and R. A. Chipman, "Mueller matrix scatter polarimetry of a diamond-turned mirror," Optical Engineering 34(6), 1593-1599 (1995).

51) J. L. Pezzaniti, S. C. McClain, R. A. Chipman, and S-Y. Lu, "Depolarization in liquid-crystal televisions," Optics Letters, 18(23), 2071-2073 (1993).

52) E. A. Sornsin, and R. A. Chipman, "Mueller matrix polarimetry of electro-optic PLZT spatial light modulators," International Symposium on Polarization Analysis and Applications to Device Technology, Proc. SPIE Vol. 2873, 196-202 (1996).

53) M. H. Smith, E. A. Sornsin, T. J. Tayag, and R. A. Chipman, "Polarization characterization of self-imaging GaAs/AlGaAs waveguide beamsplitters using Mueller matrix imaging polarimetry," Physics and Simulation of Optoelectronic Devices V, Proc. SPIE Vol. 2994, 330-338 (1997).

54) R-Y. Gerligand, R. A. Chipman, E. A. Sornsin, and M. H. Smith, "Polarization signatures of spherical and conical targets measured by Mueller matrix imaging polarimetry," Polarization: Measurement, Analysis, and Remote Sensing, Proc. SPIE Vol. 3121, 63-74 (1997).

55) B. J. DeBoo, J. M. Sasian, and R. A. Chipman, "Depolarization of diffusely reflecting man-made objects," Applied Optics, 44(26), 5434-5445 (2005).

56) A. De Martino, Y. K. Kim, E. Garcia-Caurel, B. Laude- Boulesteix, and B. Drévillon, “Optimized Mueller polarimeter with liquid crystals,” Optics Letters, 28(8), 616-618 (2003).

57) E. Garcia-Caurel, A. De Martino, and B. Drevillon, “Spectroscopic Mueller polarimeter based on liquid crystal devices,” Thin Solid Films, 455, 120-123 (2004).

58) B. Laude-Boulesteix, A. De Martino, B. Drévillon, and L. Schwartz, “Mueller polarimetric imaging system with liquid crystals,” Applied Optics, 43(14), 2824-2832(2004).

59) J. Liu, and R. M. A. Azzam, "Polarization properties of corner-cube retroreflectors: theory and experiment," Applied Optics 36(7), 1553-1559 (1997).

60) K. Crabtree, and R. Chipman, "Polarization conversion cube-corner retroreflector," Applied Optics 49(30), 5882-5890 (2010).

61) B. Bieg, “Polarization properties of a metal corner-cube retroreflector,” Fusion Engineering and Design, 96–97, 729–732 (2015).

62) R. Kalibjian, “Stokes polarization vector and Mueller matrix for a corner-cube reflector”, Optics Communications, 240(1-3), 39–68 (2004).

63) R. Kalibjian, "Output polarization states of a corner cube reflector irradiated at non-normal incidence," Optics & Laser Technology, 39(8), 1485-1495(2007).

64) I. Moreno, P. Gonzalo, and M. Strojnik, "Polarization transforming properties of Dove prisms," Optics Communications, 220(4-6), 257-268 (2003).

65) G. Yun, G. and R. A. Chipman, “Retardance in three-dimensional polarization ray tracing,” Polarization Science and Remote Sensing IV, Proc. SPIE Vol. 7461, 74610S (2009).

66) J. Kim, C. Oh, M. Escuti, L. Hosting, and S. Serati, “Wide-angle nonmechanical beam steering using thin liquid crystal polarization gratings,” Advanced Wavefront Control: Methods, Devices, and Applications VI, Proc. SPIE Vol. 7093, 709302 (2008).

67) R. Herke, M. H. Anderson, T. Baur, “Liquid Crystal in Precision Optical Devices,” Liquid Crystals III, Proc SPIE Vol. 3800, 45-51 (1999).

68) S. Harris, “Polarization effects in nematic liquid crystal optical phased arrays,” Liquid Crystals VII, Proc. SPIE Vol. 5213, 26-40 (2004).

69) I. Anisimov, S. R. Harris, B. K. Stadler, “Characterization of an optical phased array for use in free space optical communication antennas,” Free-Space Laser Communications VIII, Proc. SPIE Vol. 7091, 709105 (2008).

70) E. Hällstig, T. Martin, L. Sjöqvist, M. Lindgren, “Polarization properties of a nematic liquid-crystal spatial light modulator for phase modulation,” JOSA A, 22, 177-184 (2005).

71) J. M. López-Téllez, and N. C. Bruce, “Mueller-matrix polarimeter using analysis of the nonlinear voltage–retardance relationship for liquid-crystal variable retarders,” Applied Optics, 53(24), 5359-5366 (2014)

72) F. Bodrucki, A. Hill, J. Davis, & J. Cordell, Optical Modulation and Antialiasing Methods for Experimental Verification of Sensor Signal Integrity. IEEE Transactions on Instrumentation and Measurement, 67(1), 101-106 (2018).

73) J. Cordell, DHPC, private communication (2019).

74) M. Bass, C. DeCusatis, J. Enoch, V. Lakshminarayanan, G. Li, C. Macdonald, V. Mahajan, and E. Van Stryland, “Handbook of Optics, Volume I: Geometrical and Physical Optics, Polarized Light, Components and Instruments,” McGraw-Hill, Inc., (2009).

75) “SMS Scatterormeter Hardware Technical Reference Manual,” Schmitt Measurement Systems, Inc. (2008).

76) “SMS Scatterometer User Reference Manual,” Schmitt Measurement Systems, Inc. (2010).

77) F. E. Nicodemus, J. C. Richmond, and J.J. Hsia, “Geometrical Considerations and Nomenclature for Reflectance”, Institute for Basic Standards, National Bureau of Standards, Washington, DC (1977).

78) R. T. Holm, Handbook of Optical Constants of Solids II,” Academic Press, 2, 21-55 (1991).

79) E. A. Irene and H. Tompkins, “Handbook of Ellipsometry,” William Andrew (2005).

80) A. Laskarakis, S. Logothetidis, W. Pavlopoulou, and M. Gioti, “Mueller matrix spectroscopic ellipsometry: formulation and application,” Thin Solid Films, 455, 43-49 (2004).

81) D.C. O'Brien, G.E. Faulkner, and D.J. Edwards, "Optical Properties of a Retroreflecting Sheet," Applied Optics, 38, 4137-4144 (1999).

82) “Polarization Control with Liquid Crystals,” Meadowlark (2009).

83) J. Stockley, Boulder Nonlinear Systems, private communication (2017).